



Revealing hidden oxygen variability in the North Pacific: a two-decade analysis using GOBAI-O₂

Miho Ishizu^{1,2} and Tomomichi Ogata³

¹Center for Climate Physics, Institute for Basic Science, Busan 46241, Republic of Korea

²Pusan National University, Tonghapgyegyegwan Bldg 2 Busandaehak-ro, 63 beon-gil, Geumjeong-gu, Busan 46241, Republic of Korea

³Japan Agency for Marine–Earth Science and Technology, Research Institute for Earth and Information Sciences, 3173-25 Showa-machi, Kanagawa-ku, Yokohama 236-0001, Japan

Correspondence: Miho Ishizu (mishizu@pusan.ac.kr)

Received: 10 June 2025 – Discussion started: 28 July 2025

Revised: 17 May 2026 – Accepted: 26 May 2026 – Published: 22 June 2026

Abstract. Oceanic dissolved oxygen concentrations are thought to be declining under ongoing global warming, yet their variability remains less well understood than that of physical parameters such as temperature and salinity, primarily due to the limited spatial and temporal coverage of oxygen observation. Here, we examine linear trends in potential temperature, salinity, and dissolved oxygen in the North Pacific over the past two decades (2004–2023), using the GOBAI-O₂-v2.2 dataset (Version 4.4). We compare the diagnosed oxygen trends with those of physical parameters to reveal the spatial structure of recent changes. The oxygen trends inferred from GOBAI-O₂ are broadly consistent with trends observed along ship-based hydrographic repeat lines. While basin-scale deoxygenation is evident, we also identify localized oxygen increases on specific density surfaces. By relating these patterns to the surrounding physical environment, we find that the spatial heterogeneity in oxygen trends is consistent with known oceanographic processes, including the southward retreat of the oxygen minimum layer and the northward migration of a front separating the subtropical and subarctic gyres. These results underscore the value of GOBAI-O₂ data in linking physical variability to previously unrecognized biological and biogeochemical patterns in the ocean.

1 Introduction

Over recent decades, the global ocean has experienced a decline in its dissolved oxygen inventory, a trend projected to continue through the 21st century (Keeling et al., 2010; Breitburg et al., 2018; Stramma and Schmidtko, 2021; Limburg et al., 2020; Ito et al., 2017, 2024; Kolodziejczyk et al., 2024). This deoxygenation is driven in part by reduced ocean oxygen solubility under rising sea-surface temperatures, which promotes oxygen outgassing. In addition, enhanced stratification and a slowdown of ocean circulation under global warming can reduce interior ventilation and oxygen supply (Keeling et al., 2010; Bopp et al., 2013; Ito et al., 2017). Ocean oxygen loss can negatively affect aerobic marine organisms (Pörtner and Farrell, 2008; Sampaio et al., 2021), alter biogeochemical cycles, and potentially induce climate-relevant feedback (Berman-Frank et al., 2008). Historical deoxygenation has been inferred from globally distributed observations (Helm et al., 2011; Schmidtko et al., 2017; Ito et al., 2017; Takatani et al., 2012; Sasano et al., 2015; Lauvset et al., 2022), and Earth system models have been used to simulate both historical and future changes in ocean oxygen (Bopp et al., 2013; Kwiatkowski et al., 2020; Li et al., 2020).

Observed oxygen trends have traditionally been assessed using the discrete measurements of dissolved oxygen concentration (O₂), typically obtained by Winkler titration (Winkler, 1888). These measurements are also used to calibrate electrode- and, more recently, optode-based oxygen sensors mounted on conductivity-temperature-depth (CTD) profilers

(Helm et al., 2011; Schmidtko et al., 2017; Lauvset et al., 2022). Although programs such as WOCE, CLIVAR, and GO-SHIP have collected high-quality oxygen measurements globally, repeat occupation intervals are commonly on the order of a decade, limiting the ability to robustly quantify annual to seasonal variability. Higher-frequency ship-based observations exist in a few regions (Takatani et al., 2012; Sasano et al., 2015), but their spatial coverage is limited. Consequently, despite attempts to characterize basin-scale patterns (Ito et al., 2017; Stramma et al., 2020; Kolodziejczyk et al., 2024), observational constraints have hampered a spatially and temporally comprehensive understanding of dissolved oxygen variability and trends.

Oxygen sensors were first deployed on Argo profiling floats in the mid-2000s. Since then, approximately 1800 oxygen-equipped floats have been deployed worldwide, substantially advancing the observational basis for assessing oxygen variability and trends (Sharp et al., 2023). The expansion toward a global biogeochemical (BGC) Argo network has improved sampling in regions that were previously sparsely observed (Claustre et al., 2020). In parallel, major progress has been made in calibration, adjustments, and quality control of oxygen measurements, including pre-deployment drift corrections (D'Asaro and McNeil, 2013; Johnson et al., 2015; Bittig and Körtzinger, 2015; Bushinsky et al., 2016; Drucker and Riser, 2016; Nicholson and Feen, 2017), climatology-based calibrations (Takeshita et al., 2013), in-air oxygen measurement calibrations (Körtzinger et al., 2005; Bittig and Körtzinger, 2015; Johnson et al., 2015; Bushinsky et al., 2016), post-deployment drift corrections (Johnson et al., 2017; Bittig et al., 2018a, b), and the standardized delayed-mode quality control procedures (Maurer et al., 2021). Together, these developments have reduced uncertainty and improved the consistency of optode-based $[O_2]$ measurements from Argo floats.

To date, oxygen observations from Argo floats have been used primarily in regional process studies, including air-sea oxygen exchange (Wolf et al., 2018), upper-ocean primary production (Alkire et al., 2012; Estapa et al., 2019), biological pump efficiency (Johnson and Bif, 2021), and the dynamics of the oxygen minimum zone (Udaya Bhaskar et al., 2021). Recently, Sharp et al. (2023) produced a four-dimensional gridded $[O_2]$ product, GOBAl- O_2 (Gridded Ocean Biogeochemistry from Artificial Intelligence (AI) – Oxygen). GOBAl- O_2 is constructed using machine-learning methods trained on oxygen observations and designed to reconstruct spatial patterns, seasonal cycles, and decadal variability, particularly in regions where observational data gaps coincide with high background O_2 variability.

In the North Pacific, several studies have documented heterogeneous oxygen trends. Using an objectively mapped monthly climatology of O_2 based on the World Ocean Database 2013 (WOD13) (Boyer et al., 2013), Ito et al. (2017) reported multidecadal variability and trends in dissolved O_2 in the surface-layer oxygen from 1958

to 2013. Sasano et al. (2015), using the high-frequency shipboard sections along the 137 and 165° E lines from 1987 to 2011, reported oxygen declines in the northern subtropical to subtropical-subarctic transition zones of $-0.45 \pm 0.16 \mu\text{mol kg}^{-1} \text{yr}^{-1}$ at $25.3 \sigma_\theta$ and $-0.45 \pm 0.14 \mu\text{mol kg}^{-1} \text{yr}^{-1}$ at $26.8 \sigma_\theta$, respectively. They also identified a significant oxygen increase in the tropical Oxygen Minimum Layer (OML) of $+0.36 \pm 0.004 \mu\text{mol kg}^{-1} \text{yr}^{-1}$, highlighting pronounced spatial heterogeneity in oxygen trends. At broader scales, Stramma et al. (2020) analyzed historical bottle data and reported links between oxygen variability and climate modes such as the Pacific Decadal Oscillation (PDO) and the North Pacific Gyre Oscillation (NPGO), although sparse sampling makes it difficult to robustly connect regional trends to physical mechanisms. Collectively, previous studies indicate that oxygen changes in the North Pacific can be strong, spatially non-uniform, and potentially driven by both circulation/ventilation changes and biologically mediated oxygen consumption (Sasano et al., 2015, 2018; Ito et al., 2017, 2024; Stramma et al., 2020; Kolodziejczyk et al., 2024).

Because observational opportunities to quantify trends in dissolved oxygen – together with concomitant changes in temperature and salinity – remain limited, gridded products such as GOBAl- O_2 are becoming increasingly valuable for basin-scale analyses. In this study, we use GOBAl- O_2 to quantify linear trends in potential temperature, salinity, and dissolved oxygen in the North Pacific over 2004–2023 and examine how their trends are connected in both depth and density space. We further discuss the extent to which the diagnosed oxygen trends can be interpreted in terms of physical drivers, including surface warming, stratification changes, and circulation variability in the North Pacific.

2 Data and Methods

2.1 GOBAl- O_2 dataset

We use GOBAl- O_2 -v2.2 (Version 4.4), a four-dimensional, monthly gridded product of dissolved oxygen (O_2) in the ocean interior, generated using machine learning (ML) algorithms trained on both Argo float oxygen measurements and ship-based discrete observations (Sharp et al., 2023). GOBAl- O_2 is mapped onto the temperature-salinity fields provided by the global Argo array (Roemmich and Gilson, 2009). The underlying oxygen training database combines ship-based measurements from GLODAPv2.2022 and Argo float data distributed through the Argo Global Data Assembly Centers, after quality control (Sharp et al., 2022, <https://doi.org/10.25921/z72m-yz67>).

According to Sharp et al. (2023), the float data used in GOBAl- O_2 were filtered to retain only delayed-mode adjusted profiles with quality flags of 1 (good), 2 (probably good), or 8 (interpolated/extrapolated) for pressure, temper-

ature, salinity, and dissolved oxygen. Among all available float profiles, 51.4 % underwent quality control through comparison with climatological fields from the World Ocean Atlas (WOA) or the Commonwealth Scientific and Industrial Research Organisation Regional Sea Atlas (CARS). An additional 30.3 % were evaluated using atmospheric oxygen concentration measurements, and 7.0 % were quality controlled through comparison with in-water measurements (WOD, OMS assuming an oxygen zero, or deployment-time CTD profiles). A further 5.3 % were adjusted using in-situ optode calibration based on the method of Drucker and Riser (2016), 3.3 % were adjusted by other methods, 1.9 % were unclassified, and the remaining 0.9 % were not adjusted.

The ML models predict O_2 using predictors that include absolute salinity, conservative temperature, potential density anomaly, hydrostatic pressure, bottom depth, and additional spatiotemporal covariates representing geographic, seasonal, and interannual variability. Biological processes are not explicitly parameterized in the ML framework; however spatiotemporal covariates can implicitly capture biological influences to some extent (Giglio et al., 2018).

GOBAI- O_2 is produced using two ML approaches: feed-forward networks (FNNs) and random forest regression (RFRs, (Breiman, 2001)). The final O_2 estimate at each grid point is taken as the mean of the FNN and RFR predictions. The dataset spans 2004–2023 at monthly resolution on a $1^\circ \times 1^\circ$ latitude–longitude grid, covering 86 % of the global ocean area. The product is provided on 58 vertical levels from the surface to ~ 2000 m. Sharp et al. (2023) reported 0.79 ± 0.04 % per decade decrease in the oxygen inventory of the upper 2000 m over 2004–2022. Full details of their data sources, processing, algorithm training, evaluation, and uncertainty estimation are given in Sharp et al. (2023).

2.2 Uncertainty estimates

GOBAI- O_2 provides an uncertainty estimate for each gridded O_2 value, constructed by combining independent uncertainty components in quadrature (Sharp et al., 2023):

$$u([O_2])_{\text{tot.}} = \sqrt{u([O_2])_{\text{meas.}}^2 + u([O_2])_{\text{grid.}}^2 + u([O_2])_{\text{alg.}}^2}, \quad (1)$$

where $u([O_2])_{\text{meas.}}^2$ represents measurement uncertainty of the underlying observations, $u([O_2])_{\text{grid.}}^2$ is the gridding uncertainty associated with representing a four-dimensional spatiotemporal volume by a single value, and $u([O_2])_{\text{alg.}}^2$ is the algorithmic uncertainty arising from the ML estimation. We use $u([O_2])_{\text{tot.}}$ to characterize uncertainty in O_2 and to propagate uncertainty into our oxygen trend estimates (Figs. 1–4). In most figures, we incorporate the mean uncertainty when estimating linear O_2 trends.

2.3 Vertical grid and interpolation for isopycnal analysis

GOBAI- O_2 is provided on a $1^\circ \times 1^\circ$ horizontal grid with 58 depth levels: 2.5, 10, 30, 40, 50, 60, 70, 80, 90, 100, 110, 120, 130, 140, 150, 160, 170, 182.5, 200, 220, 240, 260, 280, 300, 320, 340, 360, 380, 400, 420, 440, 462.5, 500, 550, 600, 650, 700, 750, 800, 850, 900, 950, 1000, 1050, 1100, 1150, 1200, 1250, 1300, 1350, 1412.5, 1500, 1600, 1700, 1800, 1900 and 1975 m. The enhanced near-surface vertical resolution is important for resolving strong gradients in temperature, salinity, density, and oxygen within the mixed layer (Kara et al., 2000).

For analysis performed in density space, we interpolate the original depth-level data to 1 m vertical grid using cubic spline interpolation and then evaluate linear trends on a $1^\circ \times 1^\circ \times 1$ m grid. This approach enables computation of trends as a function of latitude (1° bins) and potential density anomaly ($0.1 \sigma_\theta$ bins) (Figs. 4–7). To evaluate sensitivity to interpolation choices, we repeated the analysis using linear, shape-preserving cubic (PCHIP) interpolation and using coarser vertical grids (2 and 5 m). The resulting trend patterns show no material differences among interpolation methods (Figs. S1a, b and S2a, b in the Supplement). The 5 m grid cannot resolve densities lighter than $24.0 \sigma_\theta$ at some latitudes; however, the main features are preserved across all tested resolutions.

2.4 OFES model output

In Sect. 3.3.2, we additionally use output from the eddy-resolving OGCM for the Earth Simulator (OFES) (Masumoto et al., 2004; Masumoto, 2010; Sasaki et al., 2008) to examine the physical context of the diagnosed variability. OFES is based on the MOM3 (Pacanowski and Griffies, 2000) and uses a quasi-global domain spanning 75° S– 75° N with $0.1^\circ \times 0.1^\circ$ horizontal resolution and 54 vertical levels. The model was initialized from rest using the World Ocean Atlas 1998 (WOA98) (Boyer and Levitus, 1997), and spun up for 50 years using climatological forcing derived from NCEP-NCAR reanalysis (Kalnay et al., 1996). After spin-up, a hindcast experiment was conducted from 1950 to 2024 using daily NCEP-NCAR forcing. Here we analyze OFES output over 1950–2023.

2.5 GODAS model output

In Sect. 3.3.2, we also use temperature and salinity fields from the NCEP Global Ocean Data Assimilation System (GODAS) to complement our analysis. GODAS is a global ocean reanalysis system developed at the National Centers for Environmental Prediction (NCEP) and is based on the Modular Ocean Model version 3 (Pacanowski and Griffies, 2000). The system assimilates surface temperature profiles, XBT data, moored buoy observations, and other in situ mea-

surements using a three-dimensional variational (3DVAR) assimilation scheme (Behringer and Xue, 2004; Behringer, 2007). The GODAS reanalysis is provided on a $1^\circ \times 1^\circ$ horizontal grid with enhanced meridional resolution ($1/3^\circ$) near the equator and includes 40 vertical levels. The reanalysis spans from 1980 to the present and is widely used for climate diagnostics and ocean variability studies. In this study, we analyze GODAS density fields over the period 2003–2024 by using temperature and salinity.

3 Results

3.1 Horizontal distributions of linear trends

Figure 1 illustrates the horizontal and vertical distributions of linear trends in potential temperature, salinity, and dissolved oxygen (O_2), over 2004–2023. Positive trends in potential temperature are primarily confined to the surface layer above 200 m depth (Fig. 1a–c), with larger magnitudes at higher latitudes. In contrast, negative trends emerge below the surface in the eastern tropical area (180 – 120° W, 5 – 15° N) (Fig. 1b), extending westward and deepening with increasing depth (Fig. 1d–f). Below ~ 400 m, the spatial distributions of positive and negative temperature trends differ between the sub-arctic and subtropical gyres.

Salinity trends exhibit generally negative values throughout the surface layer (Fig. 1h–i), consistent with freshening. Localized positive salinity trends are detected in the Kuroshio–Oyashio transition area and the northwest Pacific (140 – 180° E, 20 – 50° N), as well as in the tropical region (120 – 170° E, 0 – 10° N). Additional positive trends are observed along the eastern boundary off California (130 – 199° W, 20 – 40° N). Below 200 m depth, salinity trends are weaker and broadly mirror the temperature (Fig. 1j–k). Notably, negative salinity trends are evident around the Alaska gyre (170 – 130° W, 40 – 55° N) (Fig. 1j–l), a pattern that differs from the corresponding temperature trends.

Negative trends in dissolved O_2 are widespread across the North Pacific and extend throughout much of the water column (Fig. 1o–u). Large negative trends are concentrated at higher latitudes near the surface, with their locations shifting systematically with depth. Particularly strong O_2 declines are observed along the northeastern boundary (140 – 130° W, 40 – 50° N) and within the southern subtropical region (10 – 25° N) on density surfaces between 25.2 and $26.8 \sigma_\theta$, corresponding to depths of approximately 200–600 m (Fig. 1q–s). In contrast, weak positive O_2 trends are detected below 200 m depth in the Kuroshio–Oyashio transition zone (130 – 150° E, 30 – 40° N), extending into deeper layers and spreading north-eastward across the basin (Fig. 1r–u).

Positive O_2 trends are restricted to specific regions and depths: the tropical region at ~ 100 m depth (Fig. 1p); the Alaska Gyre at 200–400 m depth (Fig. 1q–r); the western tropical region at 400–600 m depth (Fig. 1r–s); and

the Kuroshio–Oyashio transition region at similar depths (Fig. 1r–s). When examined as a function of latitude, the magnitudes of negative O_2 trends do not depend monotonically on latitude alone. While surface-layer declines are strongest at high latitudes, the largest negative trends at intermediate depths (400–600 m) occur in the mid-latitude band (30 – 40° N). This depth-dependent latitudinal structure implies the importance of remote transports and the circulation-driven redistribution of oxygen, rather than purely local surface forcing. The underlying mechanisms are discussed further in Sect. 3.3.

The total uncertainty in dissolved O_2 , $u([O_2])_{\text{tot.}}$, exhibits pronounced regional structure (Fig. 2a–g). Uncertainty is largest in the North Pacific north of 50° N and decreases toward lower latitudes. Relatively high uncertainty values are also evident in the surface layer, and within regions of strong density gradients in the eastern tropical Pacific [150 – 120° W, 10 – 30° N] at depths of 100–200 m (Fig. 2b–c). In general, uncertainty peaks near 100 m depth and decreases with increasing depth (Figs. 2 and A14 in Sharp et al. (2023)). As shown by Sharp et al. (2023), regional variations in uncertainty are dominated by algorithmic uncertainty rather than measurement or gridding components (Eq. 1). Elevated algorithmic uncertainty in the northern Pacific above 50° N and along the western and eastern tropical margins below 20° N reflects sparse observational coverage in these regions (Fig. 1 in Sharp et al., 2023).

To assess whether regional trends exceed the dataset uncertainty, we computed the spatial distribution of Robustness (R), defined as $R = |\text{trend over two decades}|/\text{uncertainty}$ (Fig. 1v–bb). (Note: This diagnostic provides a heuristic measure of the relative strength of the trend compared to the local uncertainty, rather than a formal quantification of uncertainty propagation.) The results indicate that R exceeds or approaches high values in the eastern and western tropical zones, the Kuroshio Extension region, portions of the subpolar North Pacific, and along the 27.2 – $27.4 \sigma_\theta$ density surfaces at 800–1000 m depth. Based on this metric, larger oxygen trend magnitudes correspond to higher R values, more clearly distinguishable from the background uncertainty. Thus, in the upper ocean (2.5–100 m), trends are relatively robust in terms of the R metric, mainly in the northern North Pacific. At 200–400 m, robust signals appear both in the northern North Pacific and along the 25.2 – $26.0 \sigma_\theta$ surfaces in the southern subtropical region, as well as in the eastern and western tropics. At 600–1000 m, the trends are robust within the subtropical gyre bounded by the $27.0 \sigma_\theta$ surface.

Compared with the previously reported historical horizontal distributions of dissolved O_2 reported by Ito et al. (2017) (Fig. 3 in Ito et al., 2017), our analysis shows a broader spatial extent of negative trends across the North Pacific. Whereas data gaps increase with depth in Ito et al. (2017), the GOBAI- O_2 product provides more spatially continuous coverage, yielding distributions that are consistent with sur-

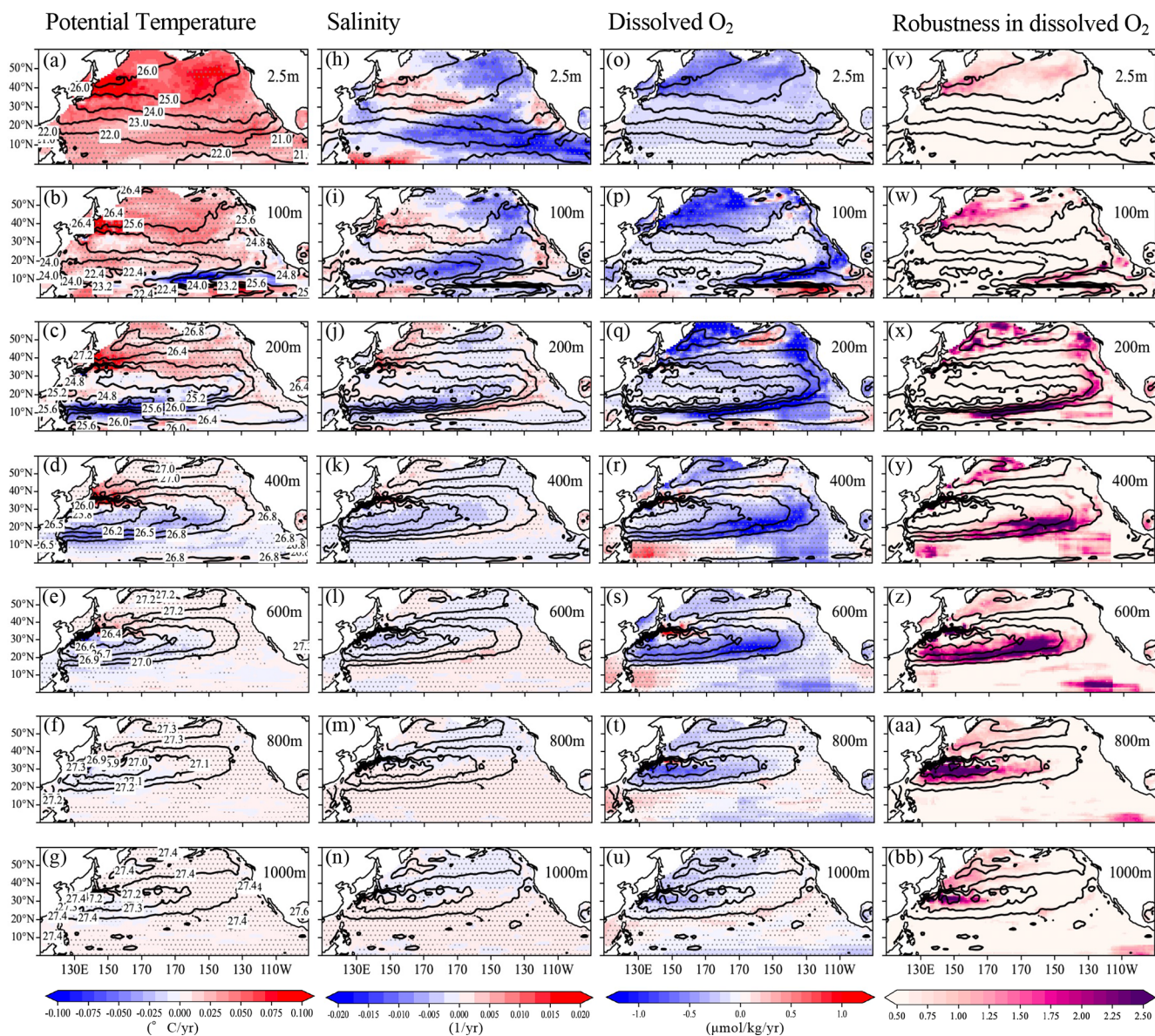


Figure 1. Horizontal distributions of linear trends in potential temperature (a–g), salinity (h–n), and dissolved oxygen (O_2) (o–u) during the observational period at depths of 0, 100, 200, 400, 600, 800, and 1000 m, respectively. Hatched areas indicate statistically significant trends at the 95 % confidence level based on a Student’s t -test with effective degrees of freedom accounting for temporal autocorrelation. Trend significance was evaluated using a Student’s t -test with effective degrees of freedom accounting for lag-1 autocorrelation. Contours denote potential density at each depth. Labels for the potential density are shown only in the potential temperature sections. Corresponding distributions of the Robustness (R), defined as the ratio of the trend magnitude to the dataset uncertainty in dissolved O_2 are presented in panels (v)–(bb).

rounding regions. In addition, positive O_2 trends detected here in the Kuroshio–Oyashio transition zone and the northeastern North Pacific on density surfaces of 26.8–27.0 σ_θ (Fig. 1r) were not clearly evident in the earlier O_2 anomaly analysis. Similarly, the positive trends identified in the western tropical Pacific below 400 m depth (Fig. 1r–t) are stronger and more spatially coherent than those reported previously.

The positive O_2 trends coincide with regions of relatively low uncertainty values (Fig. 1p–s and w–z), suggesting that they represent relatively robust features that are better constrained by the high observation density of Argo profiling floats. Other regions exhibiting positive signals – the northeastern North Pacific with a density range of 26.8–27.0 σ_θ (170° E–150° W, 45–55° N, Fig. 1r) and the tropical western Pacific (130–170° E, 0–10° N, Fig. 1r–t) – also correspond

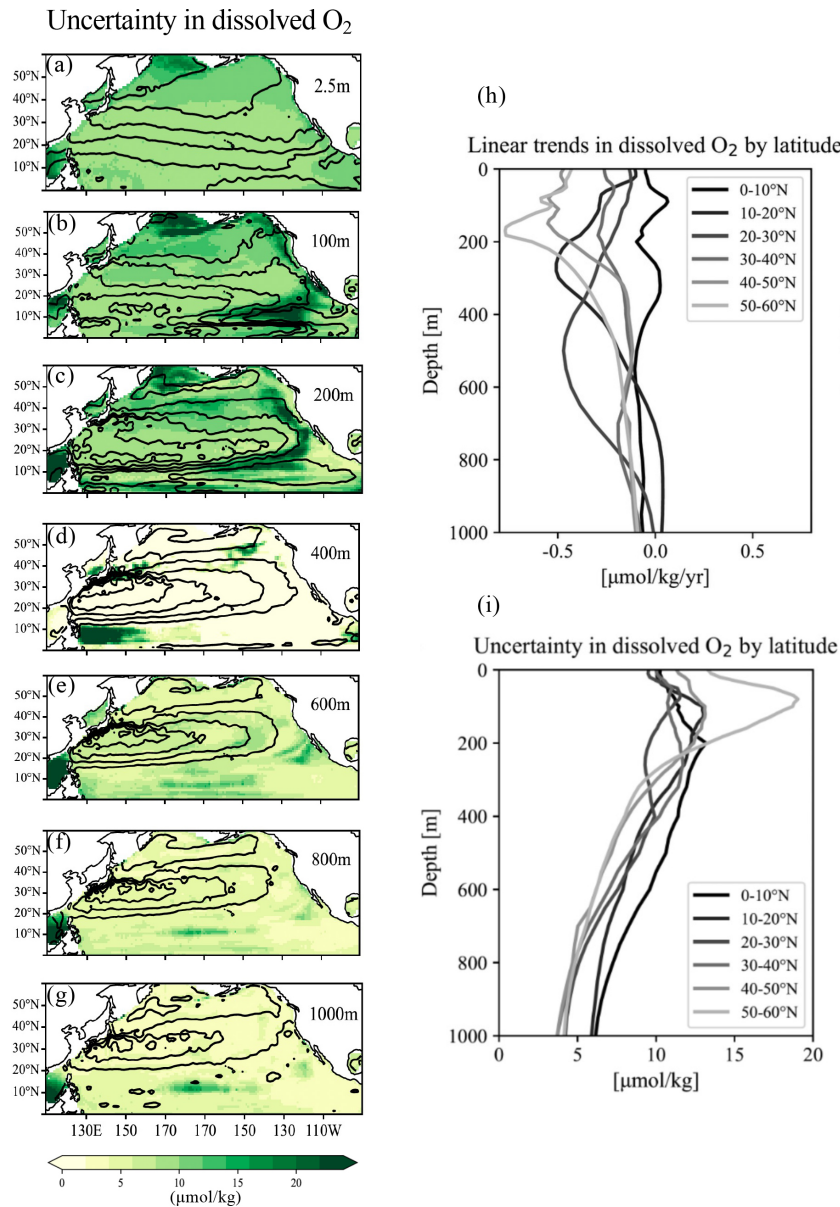


Figure 2. Horizontal distributions of dataset uncertainty in dissolved O₂ (a–g) and vertical profiles of linear trends and uncertainty in dissolved O₂ by latitude (h–i).

to areas of low uncertainty (Fig. 1y–aa). Consequently, these signals may reflect possible regional reoxygenation superimposed on the basin-scale deoxygenation trend.

Some localized expansions of the trend patterns, particularly in the tropical eastern Pacific (e.g. 170–130°W, 0–20°N) may partly reflect regions of elevated uncertainty, occasionally exceeding $15 \mu\text{mol kg}^{-1}$ (Figs. 1q–s; 4i). Such large uncertainties would likely arise from sparse observations and high background variability (Sharp et al., 2023). Additional bias may stem from sensor calibration limitations in Argo oxygen measurements, especially in oxycline regions where finite optode response times can introduce sys-

tematic errors (Bittig et al., 2014, 2018a, b). Despite these caveats, the spatial patterns of the diagnosed O₂ trends are generally smooth and coherent across the basin. Based on statistical significance testing, most trends are significant throughout the water column (Fig. 1o–u). Overall, despite the uncertainties associated with the various factors discussed above, the GOBAI-O₂ dataset provides an improved framework for diagnosing basin-scale oxygen variability and its physical drivers.

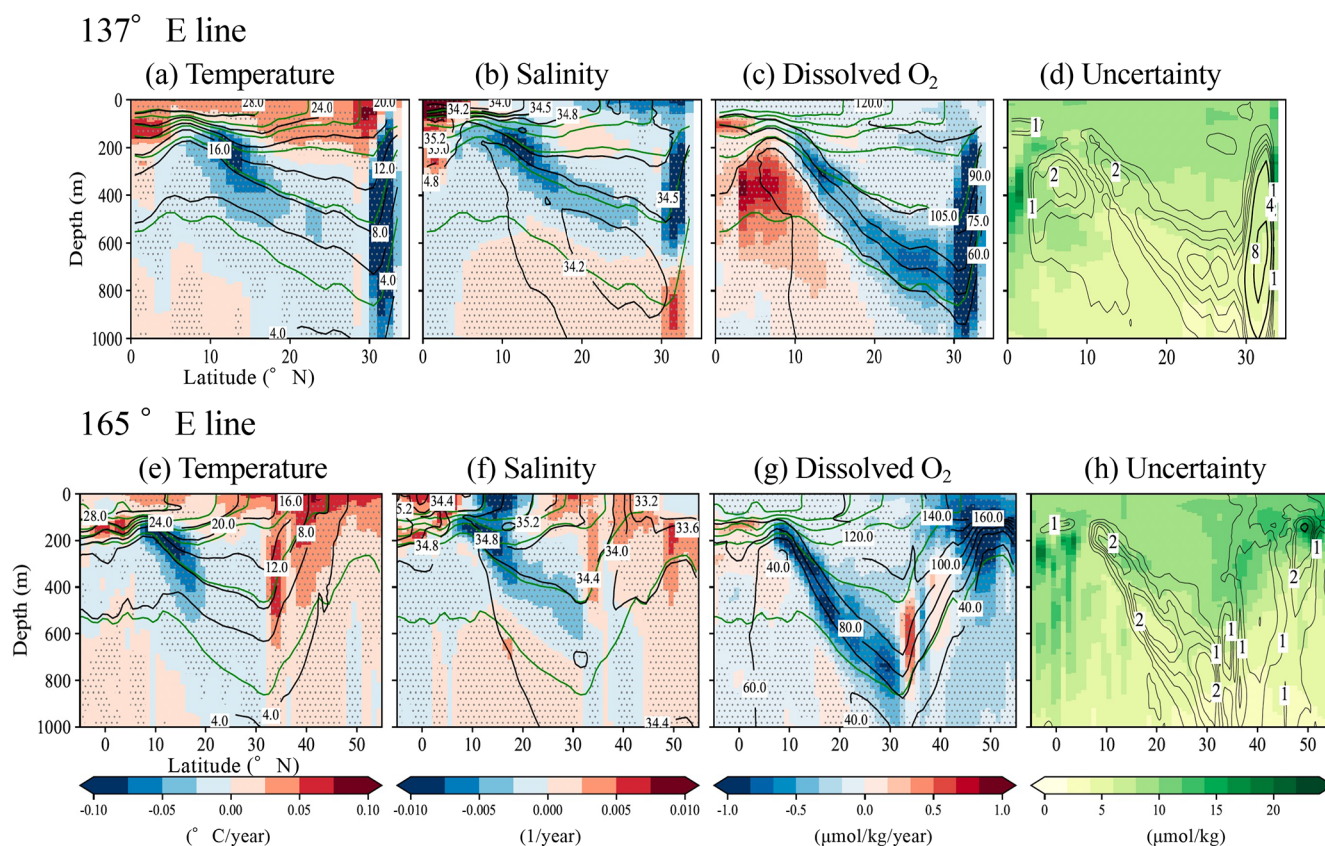


Figure 3. Vertical sections showing linear trends in potential temperature (**a, e**), salinity (**b, f**), and dissolved O_2 (**c, g**) along the 137 and 165° E meridians, respectively. Black contour lines indicate the mean potential temperature (**a, f**), salinity (**b, g**), and dissolved oxygen (**c, h**) over the period 2004–2023, while green contour lines represent the mean potential density. Labels for the potential density are shown only in the robustness sections. Hatched areas indicate statistically significant trends at the 95 % confidence level based on a Student's t -test with effective degrees of freedom accounting for temporal autocorrelation. Trend significance was evaluated using a t -test with effective degrees of freedom accounting for lag-1 autocorrelation. Corresponding vertical sections of the mean uncertainty with the contours of the Robustness (R) in panels (**d**) and (**h**). The contour intervals for thin and thick contours in (**d**) and (**h**) are 0.5 and 4.0, respectively.

3.2 Vertical sections and isopycnal density analysis of linear trends in 137 and 165° E lines

To facilitate direct comparison with historical ship-based observations, we examine vertical sections and isopycnal distributions of linear trends in potential temperature, salinity, and dissolved O_2 along the 137 and 165° E meridional sections (Fig. 3). Ogata and Nonaka (2020) analyzed salinity data from 20 years of shipboard observations along the 137° E line between 1997 and 2016, while Sasano et al. (2015) analyzed temperature, salinity, and dissolved O_2 data from 25 years of cruises along the 165° E line between 1987 and 2011.

Along both sections, large negative trends in potential temperature and salinity are concentrated along the 25.0–26.0 σ_θ isopycnal surfaces, corresponding to potential temperatures of approximately 10–12° C and salinities of 34.4–34.5 (Fig. 3a, b, e, f). In contrast, the strongest negative trends in dissolved O_2 occur primarily along denser isopycnals be-

tween 26.0 and 27.0 σ_θ (Fig. 3c, g). This vertical separation indicates that the regions of pronounced oxygen decline are not co-located with those of temperature and salinity trends, implying distinct controlling mechanisms.

In addition to widespread oxygen declines, pronounced positive O_2 trends are detected south of $\sim 15^\circ$ N below 200 m depth along the 137° E line (Fig. 3c). These positive trends are located near the upper boundary of the oxygen minimum layer (OML). Comparison with the corresponding uncertainty distributions (Fig. 3d, h) shows that regions exhibiting positive or negative oxygen trends generally do not coincide with areas of elevated uncertainty, indicating that these signals are robust within the GOBAl- O_2 framework.

The distributions of linear trends on isopycnal surfaces further highlight differences among temperatures, salinity, and dissolved O_2 (Fig. 4). Trends in temperature and salinity are closely aligned, with warming accompanied by salinification and cooling accompanied by freshening (Fig. 4a–b, d–e). In the tropical region (5° S– 5° N), distinct positive trends

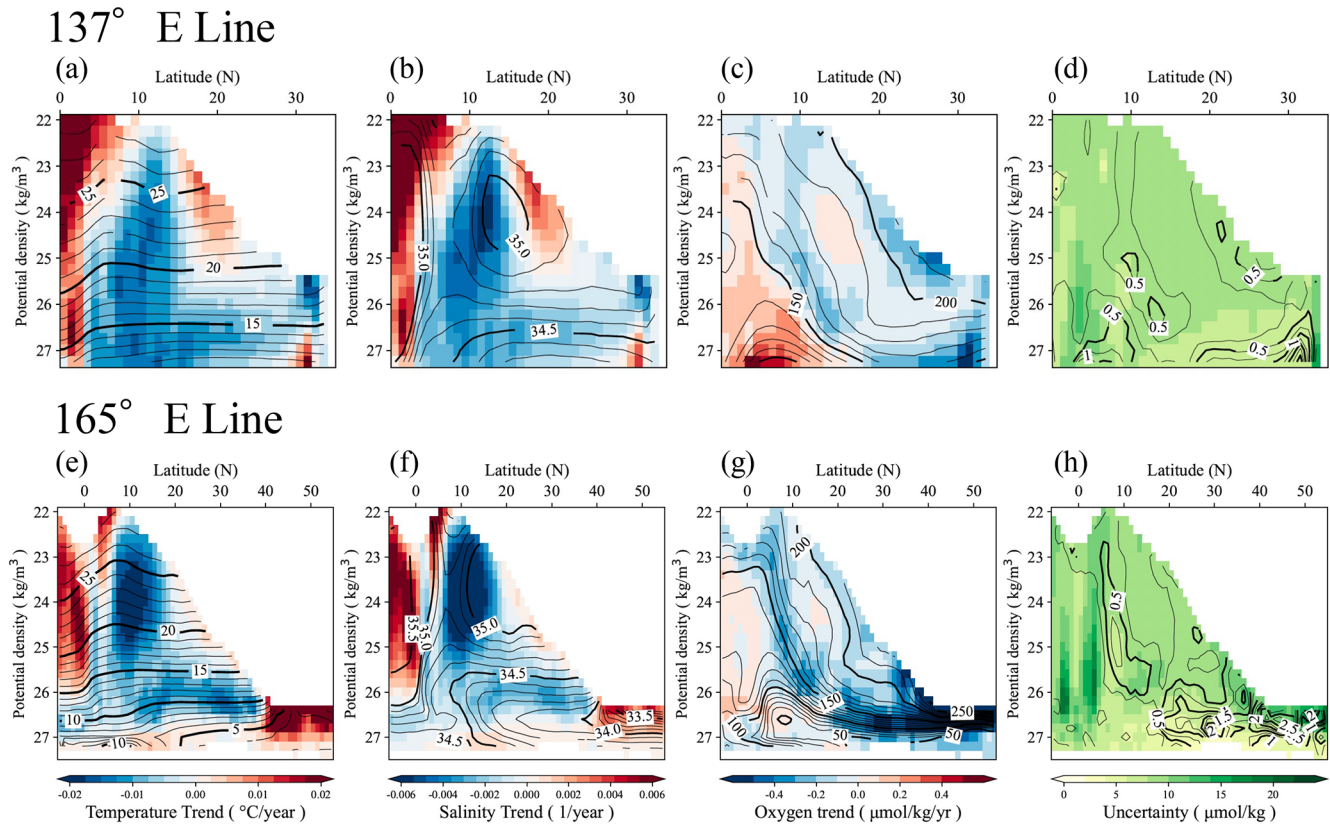


Figure 4. Linear trends in potential temperature (a, e), salinity (b, f), and dissolved O₂ (c, g) on each isopycnal surface at intervals of $0.1 \sigma_{\theta}$, calculated at every 1.0° of latitude in 137 and 165° E lines, respectively. Contour lines represent the mean values during the target observation periods, plotted at intervals of $0.1 \sigma_{\theta}$ for each 1° of latitude. Panels (d) and (h) show the corresponding vertical sections of mean uncertainty, along with contours of robustness (R). The contour intervals for thin and thick contours in (d) and (h) are 0.25 and 0.5, respectively.

in both variables are evident over the density range of 22.0 – $26.0 \sigma_{\theta}$. In contrast, little systematic trend is detected in the salinity minimum region ($S = 34$ – 34.1) within the density range of 26.5 – $27.0 \sigma_{\theta}$. At higher latitudes (40 – 50° N), strong positive trends in both temperature and salinity are observed along the 26.0 – $27.0 \sigma_{\theta}$ surfaces (Fig. 4e).

Dissolved oxygen trends exhibit a markedly different structure. Although negative O₂ trends dominate overall, weak but coherent positive trends appear across the density range 23.0 – $26.0 \sigma_{\theta}$ in low-latitude regions (5° S– 5° N). More pronounced positive O₂ trends are detected in the deeper density range of 26.0 – $27.0 \sigma_{\theta}$ between 5 and 10° N. Additional weak positive trends are observed between 10 and 20° N within the density range of 23.0 – $25.0 \sigma_{\theta}$ along both the 137 and 165° E sections.

Compared with previous studies, the GOBAI-O₂-based trends reveal both similarities and notable differences. The general characteristics of temperature and salinity trends are broadly consistent with those reported by Sasano et al. (2015), although the present results are spatially smoother, particularly for dissolved oxygen. This smoothness likely reflects the gridded nature of the dataset and the spatial reg-

ularization inherent in the machine-learning reconstruction. Along the 137° E section, the GOBAI-O₂ temperature and salinity fields exhibit a wider area of negative salinity trends within the density range 22.0 – $24.0 \sigma_{\theta}$ than those reported by Ogata and Nonaka (2020) using OFES output.

Ship-based observations by Sasano et al. (2015) identified patchy positive trends in oxygen within the density range 24.5 – $27.5 \sigma_{\theta}$ in the regions (5 – 15° N and 6° S– 1° N), as well as localized positive trends at greater depths. In contrast, the GOBAI-O₂ data reveal a broader, smoother, and more spatially coherent pattern of positive O₂ trend spanning 6° S to 5° N. At the same time, the present analysis more clearly delineates the core regions of negative oxygen trends between 5 and 15° N along the lower isopycnals (Fig. 3c, f), which are characteristic of the subtropical gyre. These differences underscore the complementary nature of ship-based observations and gridded reconstructions and highlight the advantage of GOBAI-O₂ for resolving basin-scale and isopycnal-scale oxygen variability.

3.3 Horizontal distribution of linear trends along isopycnal surfaces

3.3.1 Potential temperature and salinity

The horizontal distributions of linear trends in potential temperature, salinity, and dissolved oxygen on specific isopycnal surfaces at 25.0, 26.0, and 26.8 σ_θ (Fig. 5) are illustrated to examine how these trends occur and how they are connected. These density surfaces correspond to the shallower density range of Subtropical Mode Water (STMW), the shallower densities of Central Mode Water (CMW) (Suga et al., 1997, 2004), and the representative density of North Pacific Intermediate Water (NPIW) (Nakamura et al., 2000a, b; Nakamura and Awaji, 2004; Yasuda, 2004), respectively. STMW is formed south of the Kuroshio Extension between 30–35° N and 130–170° E, and reaches depths of approximately 400 m in late winter. It then spreads toward the subtropical front through advection across the Kuroshio recirculation area. CMW is formed in the transition area of the central North Pacific and spreads eastward along the North Pacific Current before turning southward and westward in the subtropical gyre (Suga et al., 1997, 2004). In contrast, NPIW does not outcrop during its formation process. Its origin lies in Okhotsk Sea Mode Water, which forms through overturning driven by diapycnal upwelling and tidal mixing around the Kuril Islands (Nakamura et al., 2000a, b; Nakamura and Awaji, 2004; You, 2003; Yasuda, 2004) as well as double diffusions in the North Pacific (You, 2003).

The linear trends on the 25.0, 26.0, and 26.8 σ_θ surfaces show that positive and negative tendencies appear in characteristic locations and are generally aligned with the geostrophic streamlines (Fig. 5a–b, d–e, g–h). Although exceptions exist, such as weak positive trends (150–175° E, 20–30° N) (Fig. 5a–b), negative trends in potential temperature and salinity dominate in the western and central North Pacific on the 25.0 and 26.0 σ_θ surfaces (Fig. 5a–b, d–e). Conversely, positive trends in temperature and salinity are most prevalent in the northeastern and/or eastern regions of the basin along the geostrophic streamlines (Fig. 5a–b, d–e). These patterns suggest that waters subducted in the frontal region with reduced temperature and salinity originate mainly from the northeastern North Pacific and are advected southward along the subtropical circulation (Fig. 5a–b, d–e). Exceptions occur in parts of the northeastern basin (170–130° W, 40–60° N), where warmer and more saline waters influence the water masses sinking near the Alaska gyre and subsequently transported outside the subtropical gyre and along the California coast.

At 26.8 σ_θ (Fig. 5g–h), large positive trends in temperature and salinity are found along the Kuril Islands, with moderate positive trends appearing on the eastern side of the basin, respectively. Waters at this density range (26.8 σ_θ) are not directly ventilated but are formed through diapycnal mixing processes (Nakamura et al., 2000a, b; Nakamura and Awaji,

2004; You, 2003; Yasuda, 2004) and through double diffusion such as salt fingering (You, 2003). Thus, the observed positive temperature and salinity trends at 26.8 σ_θ likely reflect influences from changes occurring in the overlying layers (Fig. 5d–e and g–h).

A meridional northward shift of the outcrop line in the North Pacific associated with recent climate change has been documented in OFES analyses (Ogata and Nonaka, 2020) and in other observational, reanalysis, and eddy-resolving ocean hindcasts (Xu et al., 2022). Consistent with these studies, the present dataset exhibits clear northward migration of the 25.0 σ_θ and 26.0 σ_θ outcrop lines (Fig. 6a), with the strong shifts occurring in the eastern basin between 150° E and 180° W (Fig. 6 and Table 1). The estimated northward shift rate at 0.004–0.09 ° yr⁻¹ from 2004 to 2023 is comparable to the value of 0.04 ° yr⁻¹ reported by Xu et al. (2022) for 1980 to 2018. Xu et al. (2022) further demonstrated that changes in the mixed layer and outcrop lines are tightly coupled with the northward migration of the North Pacific subtropical gyre and KE/OE fronts due to the poleward expansion of the Hadley cell, including the fact that the Kuroshio Extension and Oyashio Extension fronts, mode waters, and subtropical fronts evolve as a coherent system. These changes may also reflect the influence of anthropogenic warming, which has been linked to the poleward expansion of the Hadley circulation and the associated meridional shifts of oceanic fronts (Yang et al., 2020).

Such poleward displacements of frontal structures can help explain the negative temperature and salinity trends in the subtropical gyre, where less saline subarctic-origin waters are subducted and advected southward. The positive temperature and salinity trends occurring in the Alaska region (160–130° W, 30–60° N) (Fig. 5a–b and d–e) are likewise consistent with the direct surface warming. In contrast, the 26.0 σ_θ front exhibits primarily longitudinal, rather than meridional, shifts between 2004 and 2023 (Fig. 6), suggesting that the associated temperature and salinity changes arise mainly from direct surface warming and freshening, rather than from density-compensated shifts in water-mass distribution.

3.3.2 Dissolved oxygen

The linear trends in dissolved oxygen on the isopycnal surfaces at 25.0, 26.0, and 26.8 σ_θ exhibit predominantly negative values across the North Pacific (Fig. 5c, f, and i), although their spatial distributions are not uniform. Large negative trends are concentrated in the northeastern and eastern regions and gradually decrease toward the west (Fig. 5c, f, and i). Exceptions occur mainly in the tropics, where notable positive trends are found in the western tropical areas on the 26.0 and 26.8 σ_θ surfaces.

The temporal changes in dissolved oxygen (O₂) were decomposed following the method of Sasano et al. (2015). The processes underlying the oxygen tendency equations (Eqs. 2 and 3) are summarized below. We evaluated each contribut-

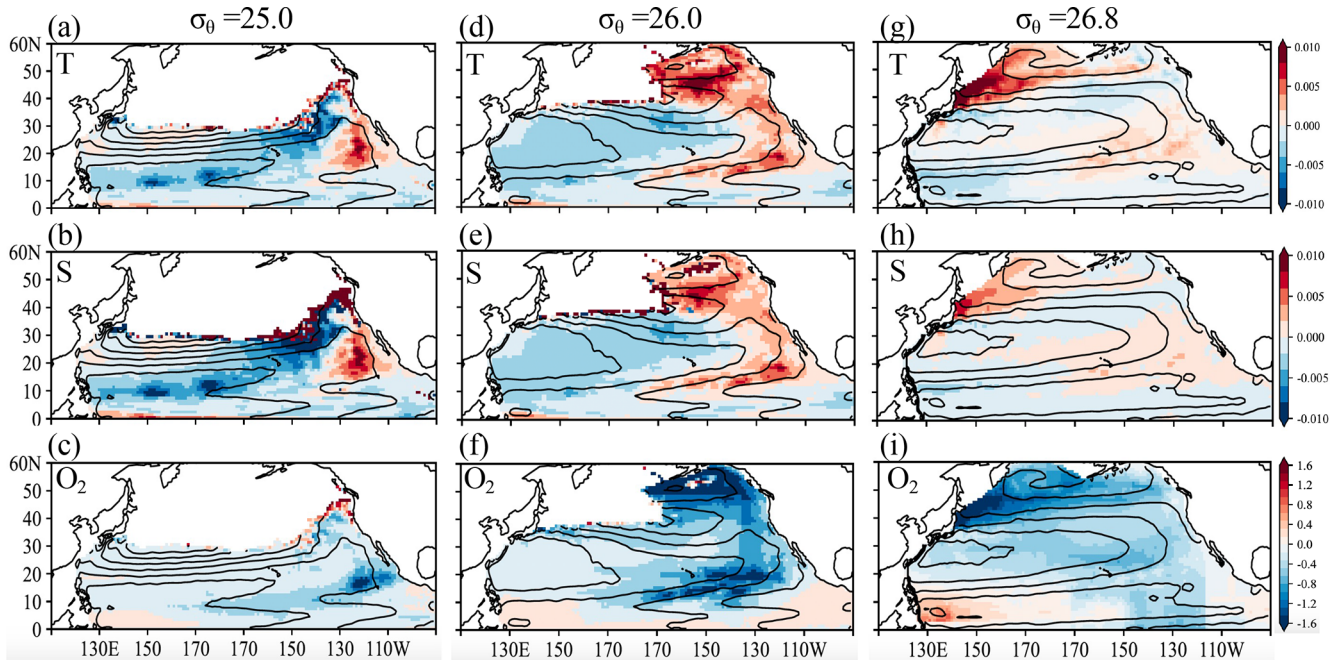


Figure 5. Linear trends in (a) potential temperature ($^{\circ}\text{yr}^{-1}$), (b) salinity (1yr^{-1}), and (c) dissolved O_2 ($\mu\text{mol kg}^{-1}\text{yr}^{-1}$) on each isopycnal surface at 25.0, 26.0, and 26.8 σ_{θ} . Contour lines represent geostrophic flow streamlines on 26.0 and 26.8 σ_{θ} surfaces, relative to 2000 m.

Table 1. Northern shifts of the (outcrop) isopycnal latitudes ($^{\circ}\text{yr}^{-1}$) for 25.0 σ_{θ} (a), 26.0 σ_{θ} (b), and 26.8 σ_{θ} (c) in the GOBAI- O_2 , OFES, and GODAS datasets. The estimates are based on data from March of each year. For 26.8 σ_{θ} , the northern shift is evaluated using the isopycnal depths corresponding to 182, 178, and 183 m in GOBAI- O_2 , OFES, and GODAS, respectively.

(a) 25.0 σ_{θ}			
Longitude	GOBAI- O_2	OFES	GODAS
150 $^{\circ}$ E	0.0241	0.0157	0.0283
170 $^{\circ}$ E	0.0444	0.0052	0.0240
170 $^{\circ}$ W	0.0684	0.0871	0.0481
150 $^{\circ}$ W	0.0947	0.0353	0.0313
130 $^{\circ}$ W	0.0420	0.0471	0.0121
(b) 26.0 σ_{θ}			
Longitude	GOBAI- O_2	OFES	GODAS
150 $^{\circ}$ E	0.0368	0.0766	0.0358
170 $^{\circ}$ E	0.0436	-0.0305	0.0508
170 $^{\circ}$ W	0.0124	0.1997	0.1412
(c) 26.8 σ_{θ}			
Longitude	GOBAI- O_2	OFES	GODAS
150 $^{\circ}$ E	0.0371	0.1980	0.0046
170 $^{\circ}$ E	0.0338	0.0217	0.1637
170 $^{\circ}$ W	0.0728	0.0054	0.0261

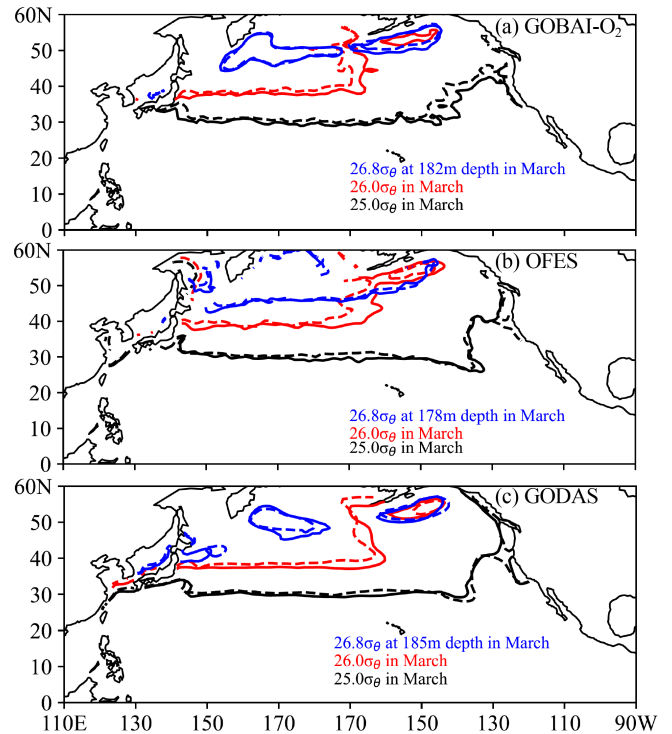


Figure 6. Density contours of 25.0 σ_{θ} (black), 26.0 σ_{θ} (red), and 26.8 σ_{θ} (blue) in each dataset: (a) GOBAI- O_2 , (b) OFES, and (c) GODAS. Solid lines indicate the mean March density contours for 2004–2009, while dashed lines represent those for 2019–2023.

ing term and examined its relative importance for the dissolved O₂ trends. The total tendency of dissolved oxygen can be expressed as

$$\frac{\partial O_2}{\partial t} = \left(\frac{\partial O_2}{\partial z} \frac{\partial z}{\partial t} \right) + \left(\frac{\partial O_2^{\text{sat}}}{\partial t} \right)_{\text{net}} - \left(\frac{\partial (\text{AOU})}{\partial t} \right)_{\text{net}}, \quad (2)$$

which can be rearranged as

$$\begin{aligned} \frac{\partial O_2}{\partial t} = & \left(\frac{\partial O_2}{\partial z} \frac{\partial z}{\partial t} \right)_{\text{(i)}} + \left(\frac{\partial O_2^{\text{sat}}}{\partial t} - \frac{\partial O_2^{\text{sat}}}{\partial z} \frac{\partial z}{\partial t} \right)_{\text{(iii)}} \\ & + \left(- \frac{\partial (\text{AOU})}{\partial t} + \frac{\partial (\text{AOU})}{\partial z} \frac{\partial z}{\partial t} \right)_{\text{(v)}}. \end{aligned} \quad (3)$$

Here, $X = O_2$, O_2^{sat} , AOU (Apparent Oxygen Utilization). The term $\partial z/\partial t$ denotes the temporal change in the depth of the isopycnal surface (z), while $\partial X/\partial z$ represents the vertical gradient of the variable X at that surface, averaged over the past 20 years. The net tendency term $(\partial X/\partial t)_{\text{net}}$ represents the net changes associated with a variable X .

By applying Eq. (3), the rate of O₂ change (term i), which is the rate of reconstructed O₂ data estimated from the linear regression analysis, on each isopycnal surface can be decomposed into contributions from:

- (term ii) vertical heave acting on the vertical O₂ gradient;
- (term iii) solubility effects due to temperature and salinity changes;
- (term iv) vertical heave acting on the solubility gradient;
- (term v) AOU changes related to air-sea disequilibrium, biological activities, and lateral circulation
- (term vi) vertical heave acting on AOU gradients.

The derivation of Eqs. (2) and (3) follows Sasano et al. (2015) and is described in Appendix A. A schematic illustration of this decomposition is provided in Fig. S5.

Figure 7 shows the horizontal distributions of the magnitude of each term on 25.0, 26.0, and 26.8 σ_θ surfaces. The results indicate that the prominent O₂ declines (Fig. 5c, f, i) arise from a combination of positive and negative contributions, with the dominant terms varying by latitude. In the high-latitude region around the Alaska Gyre (170–130° W, 40–60° N), the largest negative contributions are associated with the deepening of isopycnal surfaces (term ii) and the vertical heave acting on the AOU gradient (term vi) (Fig. 7f, j, k, o). Because the dissolved oxygen generally decreases with depth ($\partial O_2/\partial z < 0$), deepening of isopycnal surfaces ($\partial z/\partial t > 0$) (Fig. 8b–c) produces a negative contribution through vertical heave. Similarly, because AOU typically increases with depth, isopycnal deepening leads to an apparent increase in AOU, contributing negatively to dissolved O₂ via

term (vi). In contrast, solubility-related changes (term iii) and net AOU tendencies (term v) act in opposite directions during this period (Fig. 7g–h, l–m). Taken together, these results are consistent with the strong negative O₂ trends observed in the Bering Sea on the 26.0 σ_θ and 26.8 σ_θ surfaces (150° E–170° W, 50–60° N; Fig. 5f and i).

In the subtropical and mid-latitudes (10–40° N), the O₂ decline is largely associated with AOU changes (term v) (Fig. 7d, i, and n). The relative weakening of the total O₂ decrease in the western North Pacific (Fig. 5c, f, i) coincides with positive contributions from vertical heave of isopycnal surfaces (term ii) (Fig. 7f and k). Additional positive trends arise from solubility-related effects (term iii) (Fig. 7b), and the vertical heave acting on the AOU gradient (term vi) (Figs. 7j and o and 8b–c).

In the mid-ocean between 170° E and 160° W, the positive O₂ tendencies transition to weakly negative values. In contrast, a pronounced band of positive trends is found zonally across the North Pacific Ocean between 30 and 50° N, primarily associated with the combined effects of terms (iii) and (v) (Fig. 7l, h–i, and m–n). This pattern may be related to the northward meridional shift of the subtropical and subarctic frontal zone under recent global warming (Ogata and Nonaka, 2020). Enhanced winter convection in this region may introduce nutrients into the surface layer, potentially increasing biological activity and AOU. In the NPIW formation region near the Kuril Islands, negative contributions from term (iii) are observed (Fig. 7l), suggesting weaker vertical mixing during the observational period, likely influenced by enhanced surface-layer stratification. This interpretation is supported by the positive trends in temperature and salinity observed in the winter subducted areas (Suga et al., 1997, 2004; Yasuda, 2004) (Fig. 5d–e, g–h).

In the western tropical Pacific, pronounced increases in dissolved O₂ are observed within the density range of 26.8–27.2 σ_θ (Figs. 3c and g; 4c and g; 5c, f, and i), overlapping with the OML (Reid, 1997). Similar features have been reported by Sasano et al. (2015) and Takatani et al. (2012). Variability of the North Equatorial Counter Current (NECC) is likely relevant in this region. According to the study of Chen et al. (2016) based on the OFES outputs including a multidecadal variability (1960–2014), the NECC exhibits two distinct modes of variability: an interannual mode characterized by strengthening accompanied by southward migration, and an interdecadal mode marked by a gradual weakening, poleward migration, and broadening.

The validity of time-varying signals in the western tropical Pacific in the OFES data has been demonstrated by Chen et al. (2016). We further examined the longer-term OFES data (1950–2023), as well, for poleward, eastward velocities, as well as potential temperature and salinity here (Fig. 9c, g). Positive temperature anomalies in 0–5° N occur above 250 m depth, while negative anomalies appear along the 26.0 σ_θ surface between 5–20° N, a similar pattern that is also evident in the GOBAI-O₂ data (Fig. 3a). A discrepancy is found in

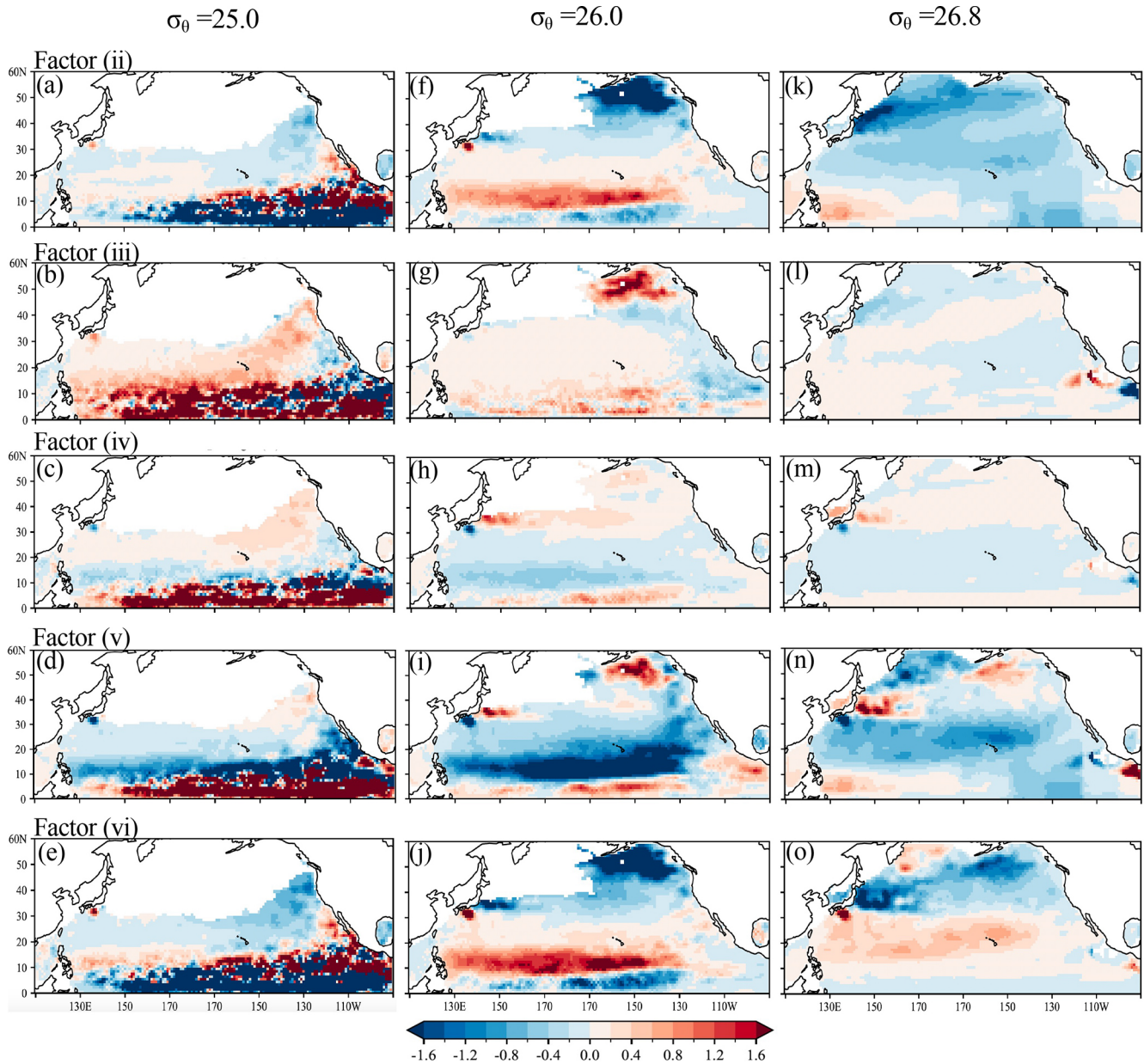


Figure 7. Horizontal distributions of the changing rates ($\mu\text{mol kg}^{-1} \text{yr}^{-1}$) of each factor contributing to the rate of O_2 change on 25.0, 26.0, and 26.8 σ_θ in Eq. (1). The rate of O_2 change on each isopycnal surface is decomposed into the following components: (ii) the apparent contribution from vertical heave (deepening or shoaling) of isopycnal surfaces associated with warming and/or surface freshening; (iii) the contribution from changes in oxygen solubility (O_2^{sat}) associated with temperature and salinity variations; (iv) the contribution from vertical heave acting on the background solubility gradient; (v) the contribution from net changes in apparent oxygen utilization (AOU) associated with air–sea disequilibrium, biological activity, and lateral advection and/or circulation; and (vi) the contribution from vertical heave acting on AOU gradients, independent of solubility changes. This decomposition is applied to the reconstructed dissolved oxygen fields obtained from linear regression analysis.

salinity trends: GOBAI- O_2 shows negative trends along 26.0 σ_θ (Fig. 3b), whereas OFES exhibits positive trends (Fig. 9b, f), likely reflecting higher salinity at 200–600 m depth in OFES between 0 and 7° N (Fig. 10b, d).

Anomalies in poleward and eastward velocities (Figs. 9a–b, e–f and 11a–b) indicate enhanced poleward flow around

5° N above 200 m depth and a poleward shift of the eastward velocity core. These changes are consistent with the interdecadal mode of NECC variability described by Chen et al. (2016). The broadening of the NECC was less evident here, possibly because the present analysis uses raw velocity fields rather than isolating the second EOF modes. The wind-stress

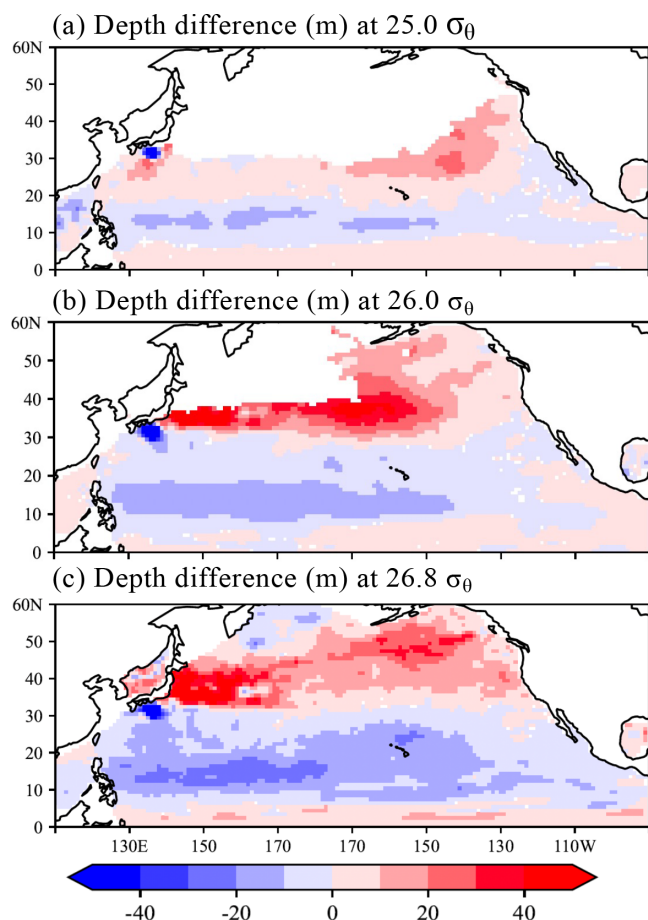


Figure 8. Depth difference (*m*) between the 5-year averaged data in March, 2004–2009 and 2018–2023 at 25.0, 26.0, and 26.8 σ_θ . The reconstructed O_2 data estimated from the linear regression analysis were used in this calculation. Positive and negative values indicate the deepening and shallowing, respectively, from the depth of each density in 2004–2023.

curl over the equatorial Pacific shows a persistent decrease and poleward expansion of negative values along the 0–10° N from 1950 to 2023 (Fig. 12).

The westward penetration of the OML is slow and occurs between two eastward-extending tongues of high O_2 water originating near the equator (Reid, 1997) (Fig. S6). The observed O_2 increase on the 26.8–27.2 σ_θ surfaces (Figs. 3c, g and 4c, g) is consistent with a weakening and northward shift of the interdecadal NECC mode. The subsurface O_2 increase, particularly below 400 m depth (Fig. 1r–u), is therefore likely influenced by these circulation changes, potentially allowing higher- O_2 water to extend westward (Fig. S6). In addition, shoaling of isopycnal surfaces near the equator indicates a northward shift of the boundary between the tropical and subtropical gyres along 137° E line during the observational period.

4 Discussion and Conclusion

The variability of dissolved oxygen in the North Pacific reflects the combined influences of global warming and climate variability. In this study, we used the four-dimensional GOBAI- O_2 dataset, constructed using machine-learning methods applied to historical temperature, salinity, and oxygen observations from BGC-Argo floats and ship-based measurements – to examine linear trends in potential temperature, salinity, and dissolved oxygen over the past two decades (2004–2023). The linear trends are broadly consistent with findings from previous studies (Takatani et al., 2012; Sasano et al., 2015; Ogata and Nonaka, 2020), and we clarified how these trends vary spatially (Figs. 3 and 4).

An important outcome of this study is that GOBAI- O_2 , being globally gridded, allows spatially continuous and smooth representations of trends, both horizontally and vertically, across the North Pacific. This provides a more spatially coherent representation than earlier datasets that relied solely on sparse ship-based observations. The horizontal trend patterns mapped on isopycnal surfaces (Fig. 5) show that dissolved oxygen exhibits a basin-scale decreasing trend. At the same time, several regions display locally increasing oxygen, including areas influenced by the meridional migration of subtropical and subpolar fronts (Fig. 4). The strong positive oxygen trends in the western equatorial region are consistent with a weakening of the second mode of the NECC variability. The decomposition analysis further illustrates how each physical component contributes to oxygen changes along isopycnal surfaces (Fig. 7).

Although many of the large-scale features identified here resemble those reported by Ito et al. (2017), our analysis reveals regional and isopycnal-scale structures that were previously unresolved. In particular, the positive oxygen trends in the Kuroshio–Oyashio Transition Zone, the northeastern North Pacific along the 26.8–27.0 σ_θ density surfaces, and the enhanced subsurface O_2 increase in the tropical western Pacific below 400 m were not clearly distinguished in earlier O_2 anomaly studies. These improvements arise because GOBAI- O_2 integrates high-frequency BGC-Argo oxygen observations with a spatially consistent mapping scheme, reducing observational gaps and sampling biases in dynamically active regions. This suggests that regional reoxygenation signals can coexist with large-scale deoxygenation, and highlights the importance of sustained BGC-Argo observations for detecting emerging changes in ocean biogeochemistry.

Recent work by Bushinsky et al. (2025) has reported the presence of a systematic negative bias (approximately $-2.7 \mu\text{mol kg}^{-1}$) in air-calibrated BGC-Argo oxygen measurements compared with ship-based reference profiles. This bias does not appear to be explicitly corrected in version 4.4 of GOBAI- O_2 -v2.2 and may therefore influence the magnitude of the estimated oxygen trends—potentially enhancing negative trends or suppressing positive ones in regions with

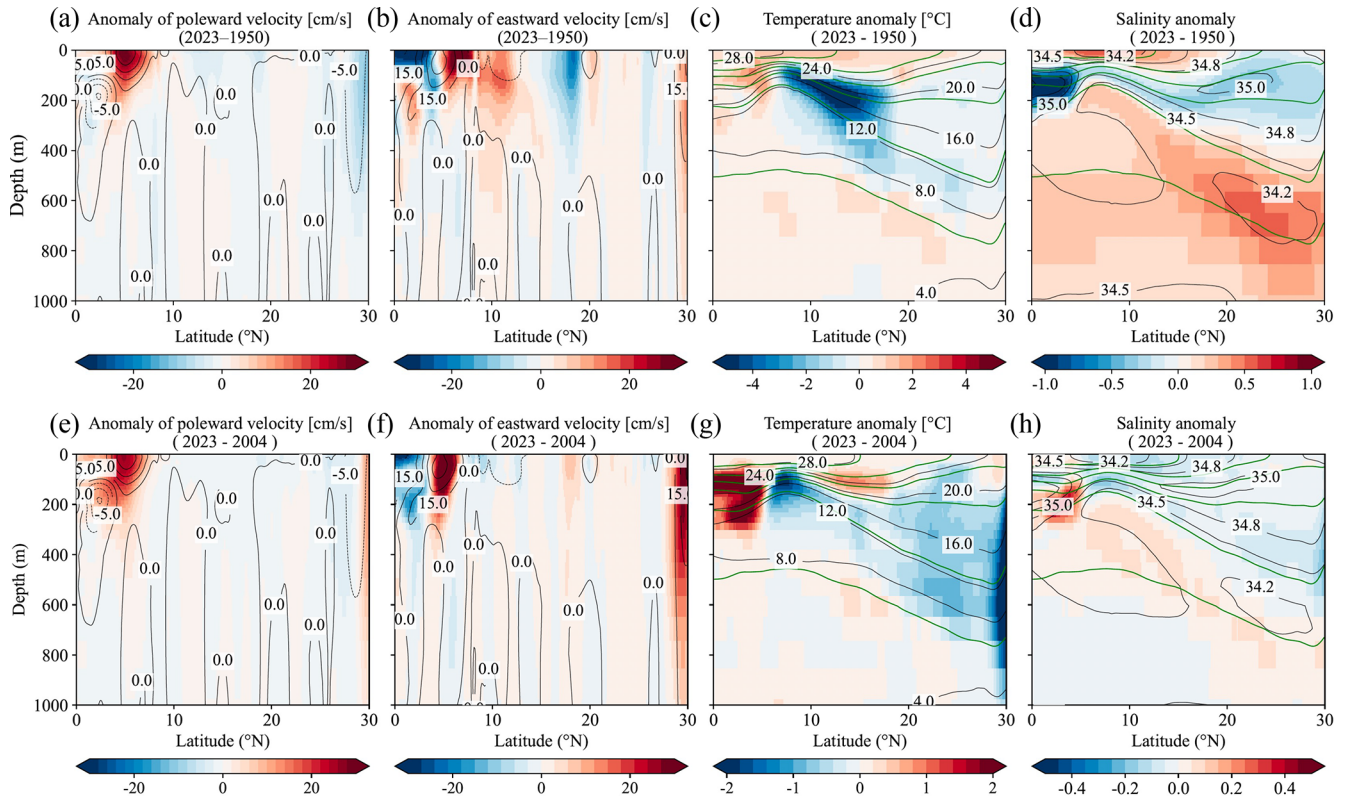


Figure 9. Anomaly of poleward and eastward velocity, potential temperature, and salinity in the OFES model outputs from 1950 to 2023 (a–d) and from 2004 to 2023 (e–h), respectively, in the 137° E line. Contours of averaged values of poleward and eastward velocity, potential temperature, and salinity during the target period are also shown in each figure. Green contour lines in (c)–(d), (g)–(h) indicate the average potential density of 22, 23, 24, 25, 26, and 27 σ_θ , during the target periods.

dense float sampling. However, as described in Sect. 2.1, a substantial fraction of these float data is subject to quality control through comparison with climatological fields derived from ship-based discrete observations, and only profiles with appropriate quality flags are retained and incorporated into the dataset development. While this filtering procedure likely mitigates a portion of the air-calibration bias, the extent to which residual bias remains in the reconstructed fields is not well quantified.

If present, such biases could also affect the apparent vertical structure of the oxycline. In the North Pacific, regions with high float density—such as the Kuroshio–Oyashio transition zone, the North American coastal region, and the vicinity of Hawaii—may be particularly affected (see Fig. 1 of Sharp et al., 2023). While a constant offset would not directly alter linear trend estimates, any time-varying bias associated with sensor behavior or sampling depth could introduce spurious trends. A quantitative evaluation is not feasible at present due to the lack of temporally continuous ship-based reference data at the spatial scales. This limitation should therefore be kept in mind when interpreting the O_2 trends reported here. Accordingly, the interpretation of the diagnosed

O_2 trends should be made with caution, particularly in regions where float-based observations dominate.

It is also essential to recognize that GOBAI- O_2 is a machine learning reconstruction derived from available temperature, salinity, and oxygen measurements. While this approach significantly enhances spatial coverage, the results should be interpreted cautiously. In particular, although the large-scale spatial patterns are broadly consistent across datasets, both the magnitude of trends and finer-scale spatial features may still be affected by unresolved observational and reconstruction uncertainties. Nevertheless, future work incorporating improved calibration of Argo oxygen sensors, expanded ship-based reference datasets, independent machine learning reconstructions (e.g., Ito et al., 2024), and comprehensive ocean reanalysis will be necessary to better constrain these uncertainties.

Different versions of the GOBAI- O_2 product may yield different oxygen trend estimates because of methodological differences among releases. Therefore, some of the regional patterns discussed in this study may be sensitive to the specific GOBAI- O_2 version used in the analysis. Future comparisons across multiple GOBAI- O_2 versions and observational

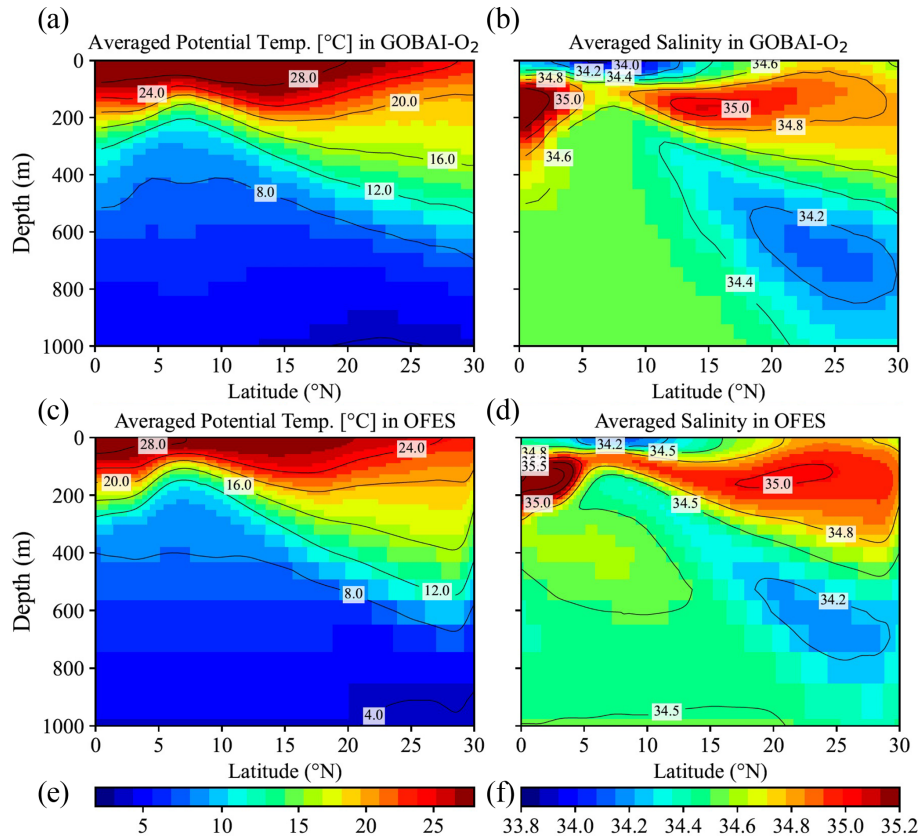


Figure 10. Averaged Potential Temperature (a, c) and salinity (b, d) in GOBAI-O₂ from 2004 to 2023 and OFES data from 1950 to 2023, respectively, in the 137° E line.

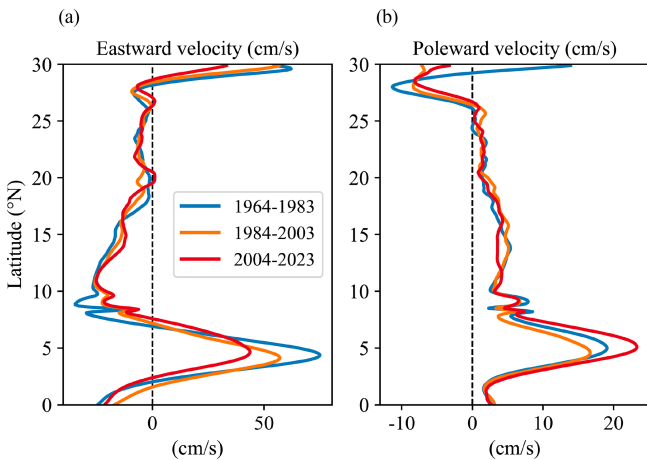


Figure 11. Latitudinal distribution of averaged eastward (a) and poleward velocity (b) in the OFES data from 1964 to 1983, from 1984 to 2003, and from 2004 to 2023, respectively, in the 137° E line.

products would help further assess the robustness of the results.

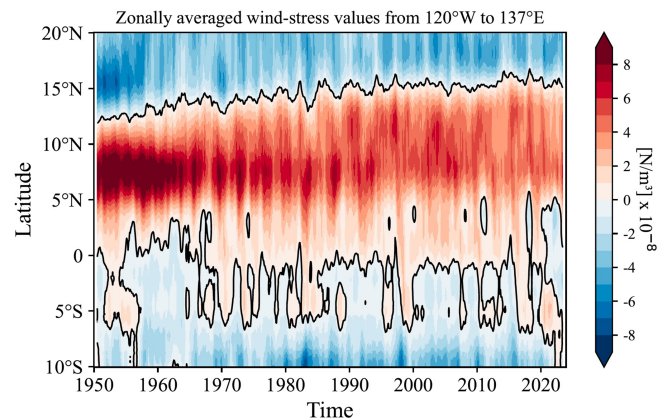


Figure 12. NCEP-NCAR wind-stress curl values zonally averaged from 137° E to 120° W from 1950 to 2023. A 13-month running-mean filter has been applied in time.

The monthly mean climatological GOBAI-O₂ dataset should include the Pacific Decadal Oscillation (PDO; Stramma et al., 2020; Pozo Buil and Di Lorenzo, 2017) and the North Pacific Gyre Oscillation (NPGO; Stramma et al., 2020). This dataset, therefore, provides a valuable basis for

examining how such climate variability influences dissolved oxygen through physical driving mechanisms. Investigating these relationships more explicitly will be an important direction for future research.

Appendix A: Essential concepts and derivations for Eqs. (2)–(3)

The essential concepts and derivations for Eqs. (2) and (3) were originally proposed by Takatani et al. (2012) and subsequently described in detail by Sasano et al. (2015). Here, we briefly summarize and follow their derivation.

When the temperature at a depth z_A increases from θ_A to θ'_A as a result of increased ocean heat content, the density at that depth decreases from σ_A to σ'_A . For simplicity, the vertical salinity profile is assumed to remain unchanged with time. As a consequence, the isopycnal surface of σ_A deepens from z_A to z_B (Fig. S5). If surface freshening occurs simultaneously due to a net freshwater input, both the density decreases at z_A (from σ_A to σ'_A) and the deepening of the isopycnal surface (from z_A to z_B) are enhanced. Because density is a function of temperature and salinity ($\sigma = f(\theta S)$), the density of the isopycnal surface σ_A can be expressed as

$$\sigma_A = f(\theta_A S_A) \text{ (before warming)} \quad (\text{A1})$$

$$= f(\theta'_B, S_B) \text{ (after warming)}. \quad (\text{A2})$$

Here, S_A and S_B denote salinity at depth z_A and z_B , respectively, and θ'_B represents the temperature at density σ_A at depth z_B after warming. The depth z_B is determined by satisfying Eqs. (A1) and (A2). In the region where salinity decreases with depth (e.g., above the salinity minimum layer of NPIW), $S_A > S_B$, and therefore $\theta_A > \theta'_B$. This implies that the potential temperature on an isopycnal surface effectively decreases as a consequence of warming, and that biogeochemical properties on the same isopycnal surface are also expected to change.

For a tracer X whose vertical profile with respect to depth does not change with time (e.g., salinity; see Fig. S5c), the temporal change of X on the potential density surface σ_A is attributed solely to the apparent change caused by the deepening of the isopycnal surface from z_A to z_B :

$$\frac{\partial X}{\partial t} = \left(\frac{\partial X}{\partial z} \cdot \frac{\partial z}{\partial t} \right) \quad (\text{A3})$$

Here, $\partial X/\partial t$ represents the temporal change of X observed on σ_A (gray arrows in Fig. S5), z denotes the depth of σ_A , $\partial X/\partial z$ is the vertical gradient of X with respect to the depth (assumed to be time-invariant), and $\partial z/\partial t$ is the rate of deepening of the isopycnal surface σ_A . The product $\partial X/\partial z \cdot \partial z/\partial t$ represents the effect of isopycnal deepening (white arrows in Fig. S5), corresponding to the difference between the filled square and filled circle.

For a variable Y whose vertical profile evolves with time while warming occurs simultaneously, the temporal change

of Y on the density surface σ_A can be expressed as the sum of two components: the contribution due to the isopycnal deepening from z_A to z_B and the net temporal change of Y , $(\partial Y/\partial t)_{\text{net}}$ between the time before and after warming:

$$\frac{\partial Y}{\partial t} = \left(\frac{\partial Y}{\partial z} \cdot \frac{\partial z}{\partial t} \right) + \left(\frac{\partial Y}{\partial t} \right)_{\text{net}} \quad (\text{A4})$$

To evaluate the net change $(\partial Y/\partial z)_{\text{net}}$ (illustrated by the blue arrows of a difference in symbols between filled square and open square in Fig. S5), it is necessary to evaluate the contribution of the temporal change of Y due to the isopycnal deepening and to subtract it from the change of Y observed at density σ_A . For instance, the change of O_2^{sat} in Fig. S5f is observed along the gray isopycnal surface (large white arrow), whereas the net change (large blue and pink arrows) is obtained as the difference between the observed change and the deepening effect.

The dissolved oxygen concentration O_2 can be expressed as:

$$\text{O}_2 = \text{O}_2^{\text{sat}} - \text{AOU}, \quad (\text{A5})$$

where O_2^{sat} is the oxygen saturation concentration (a function of temperature and salinity), and AOU is “apparent oxygen utilization”, representing the oxygen consumed by biological processes since subduction. Near the surface, AOU is typically small, and its contributions can be neglected.

Following Eq. (A4), the temporal change of O_2 on a given isopycnal surface at a fixed station is:

$$\frac{\partial \text{O}_2}{\partial t} = \left(\frac{\partial \text{O}_2}{\partial z} \cdot \frac{\partial z}{\partial t} \right) + \left(\frac{\partial \text{O}_2}{\partial t} \right)_{\text{net}}. \quad (\text{A6})$$

Similarly,

$$\frac{\partial \text{O}_2^{\text{sat}}}{\partial t} = \left(\frac{\partial \text{O}_2^{\text{sat}}}{\partial z} \cdot \frac{\partial z}{\partial t} \right) + \left(\frac{\partial \text{O}_2^{\text{sat}}}{\partial t} \right)_{\text{net}}, \quad (\text{A7})$$

and

$$\frac{\partial \text{AOU}}{\partial t} = \left(\frac{\partial (\text{AOU})}{\partial z} \cdot \frac{\partial z}{\partial t} \right) + \left(\frac{\partial (\text{AOU})}{\partial t} \right)_{\text{net}}. \quad (\text{A8})$$

The term net is directly related to warming, because depends on temperature and salinity. If AOU does not change with time, that is, if changes in O_2 arise solely from changes in, then $\partial (\text{AOU})/\partial t$ follows Eq. (A3) and $= 0$. If AOU varies with time, however, $\partial (\text{AOU})/\partial t$ follows Eq. (A4) and $\neq 0$, as illustrated by the dashed gray line in Fig. S5g.

Because O_2 is defined by Eq. (A5), the net temporal change of O_2 on an isopycnal surface is

$$\left(\frac{\partial \text{O}_2}{\partial t} \right)_{\text{net}} = \left(\frac{\partial \text{O}_2^{\text{sat}}}{\partial t} \right)_{\text{net}} - \left(\frac{\partial (\text{AOU})}{\partial t} \right)_{\text{net}}. \quad (\text{A9})$$

Combining Eqs. (A6) and (A9), the total temporal change of O_2 on an isopycnal surface can be written as

$$\left(\frac{\partial \text{O}_2}{\partial t} \right) = \left(\frac{\partial \text{O}_2}{\partial z} \cdot \frac{\partial z}{\partial t} \right) + \left(\frac{\partial \text{O}_2^{\text{sat}}}{\partial t} \right)_{\text{net}} - \left(\frac{\partial (\text{AOU})}{\partial t} \right)_{\text{net}}, \quad (\text{A10})$$

which corresponds to Eq. (1) in the main text. Equation (A10) corresponds to an arrow in Fig. S5e, represented from left to right by the large gray arrow, white, blue, and pink arrows. The large blue arrow is identical to Fig. S5f, while the large pink arrow corresponds to Fig. S5g, but with its direction reversed. Finally, substituting Eqs. (A7) and (A8) into (A10)

$$\frac{\partial O_2}{\partial t} = \underbrace{\left(\frac{\partial O_2}{\partial z} \frac{\partial z}{\partial t}\right)}_{(i)} + \underbrace{\left(\frac{\partial O_2^{\text{sat}}}{\partial t} - \frac{\partial O_2^{\text{sat}}}{\partial z} \frac{\partial z}{\partial t}\right)}_{(ii)} - \underbrace{\left(\frac{\partial(\text{AOU})}{\partial t} - \frac{\partial(\text{AOU})}{\partial z} \frac{\partial z}{\partial t}\right)}_{(iii)}, \quad (\text{A11})$$

which corresponds to Eq. (2) in the main text. Note: The signs in terms (v) and (vi) in Eq. (3) are reversed relative to those in Eq. (A11) for convenience.

Table A1. The physical interpretation of each term in the oxygen tendency decomposition shown in Eqs. (3) and (A11) is summarized.

Term	Mathematical form	Physical interpretation
(ii)	$(\partial O_2 / \partial z)(\partial z / \partial t)$	Vertical heave acting on the O_2 gradient
(iii)	$\partial O_2^{\text{sat}} / \partial t$	Solubility effect due to temperature and salinity changes
(iv)	$-(\partial O_2^{\text{sat}} / \partial z)(\partial z / \partial t)$	Vertical heave acting on the solubility gradient
(v)	$\partial \text{AOU} / \partial t$	AOU changes related to air-sea disequilibrium, biological activity and lateral circulation
(vi)	$-(\partial \text{AOU} / \partial z)(\partial z / \partial t)$	Vertical heave of the AOU gradient

Data availability. GOBAI- O_2 data is available at <https://www.ncei.noaa.gov/access/metadata/landing-page/bin/iso?id=gov.noaa.nodc:0259304> (last access: 16 June 2026). Temperature and salinity are from Roemmich and Gilson (2009) Argo climatology (https://sio-argo.ucsd.edu/RG_Climatology.html, last access: 16 June 2026). The OFES, NCEP-NCAR, and GODAS data used in our study are obtained from APDRC, University of Hawaii (<https://apdrc.soest.hawaii.edu/data/data.php>, last access: 16 June 2026).

Supplement. The supplement related to this article is available online at <https://doi.org/10.5194/bg-23-4037-2026-supplement>.

Author contributions. MI designed the study, performed the analyses, and prepared all figures. MI wrote the initial draft of the

manuscript. MI and TO contributed to the interpretation of the results. All authors contributed to improving the manuscript.

Competing interests. The contact author has declared that neither of the authors has any competing interests.

Disclaimer. Publisher's note: Copernicus Publications remains neutral with regard to jurisdictional claims made in the text, published maps, institutional affiliations, or any other geographical representation in this paper. The authors bear the ultimate responsibility for providing appropriate place names. Views expressed in the text are those of the authors and do not necessarily reflect the views of the publisher.

Acknowledgements. Jonathan D. Sharp and the reviewers are acknowledged for providing comments that prompted significant improvements to this manuscript.

Financial support. This research was supported by the Institute for Basic Science South Korea (grant no. IBS-R028-D1) and the Japan Society for the Promotion of Science Japan (JSPS) through Grants-in-Aid for Scientific Research (grant nos. 22H00176, 26K07196, and 26K07251).

Review statement. This paper was edited by Koji Suzuki and reviewed by two anonymous referees.

References

- Alkire, M. B., D'Asaro, E., Lee, C., Perry, M. J., Gray, A., Cetinić, I., Briggs, N., Rehm, E., Kallin, E., Kaiser, J., and González-Posada, A.: Estimates of net community production and export using high-resolution, Lagrangian measurements of O_2 , NO_3^- , and POC through the evolution of a spring diatom bloom in the North Atlantic, *Deep-Sea Res. Pt. I*, 64, 157–174, <https://doi.org/10.1016/j.dsr.2012.01.012>, 2012.
- Behringer, D. W. and Xue, Y.: Evaluation of the global ocean data assimilation system at NCEP: The Pacific Ocean, 8th Symposium on Integrated Observing and Assimilation Systems for Atmosphere, Oceans, and Land Surface, AMS 84th Annual Meeting, Washington State Convention and Trade Center, Seattle, Washington, 11–15, <https://ams.confex.com/ams/pdfpapers/70720.pdf> (last access: 16 June 2026), 2004.
- Behringer, D. W.: The Global Ocean Data Assimilation System (GODAS) at NCEP, 11th Symposium on Integrated Observing and Assimilation Systems for Atmosphere, Oceans, and Land Surface, San Antonio, TX, American Meteorological Society, 3.3, <https://ams.confex.com/ams/pdfpapers/119541.pdf> (last access: 16 June 2026), 2007.
- Berman-Frank, I., Chen, Y. B., Gao, Y., Fennel, K., Follows, M. J., Milligan, A. J., and Falkowski, P. G.: Feedbacks between the nitrogen, carbon and oxygen cycles, in: *Nitrogen in the Marine En-*

- vironment, Elsevier Inc., 1539–1563, ISBN 978-0-12-372522-6, 2008.
- Bittig, H. C., Fiedler, B., Scholz, R., Krahnemann, G., and Körtzinger, A.: Time response of oxygen optodes on profiling platforms and its dependence on flow speed and temperature, *Limnol. Oceanogr.-Meth.*, 12, 617–636, <https://doi.org/10.4319/lom.2014.12.617>, 2014.
- Bittig, H. C. and Körtzinger, A.: Tackling Oxygen Optode Drift: Near-Surface and In-Air Oxygen Optode Measurements on a Float Provide an Accurate in Situ Reference, *J. Atmos. Ocean. Tech.*, 32, 1539–1553, <https://doi.org/10.1175/JTECH-D-14-00162.1>, 2015.
- Bittig, H. C., Körtzinger, A., Neill, C., van Ooijen, E., Plant, J. N., Hahn, J., Johnson, K. S., Yang, B., Emerson, S. R., Krahnemann, G., and Riser, S. C.: Oxygen Optode Sensors: Principle, Characterization, Calibration, and Application in the Ocean, *Front. Mar. Sci.*, 4, 429, <https://doi.org/10.3389/fmars.2017.00429>, 2018a.
- Bittig, H. C., Steinhoff, T., Claustre, H., Fiedler, B., Williams, N. L., Sauzède, R., Körtzinger, A., and Gattuso, J.-P.: An Alternative to Static Climatologies: Robust Estimation of Open Ocean CO₂ Variables and Nutrient Concentrations From T, S, and O₂ Data Using Bayesian Neural Networks, *Frontiers in Marine Science*, 5, 328, <https://doi.org/10.3389/fmars.2018.00328>, 2018b.
- Bopp, L., Resplandy, L., Orr, J. C., Doney, S. C., Dunne, J. P., Gehlen, M., Halloran, P., Heinze, C., Ilyina, T., Séférian, R., Tjiputra, J., and Vichi, M.: Multiple stressors of ocean ecosystems in the 21st century: projections with CMIP5 models, *Biogeosciences*, 10, 6225–6245, <https://doi.org/10.5194/bg-10-6225-2013>, 2013.
- Boyer, T. P. and Levitus, S.: Objective Analyses of Temperature and Salinity for the World Ocean on a 1/4° Grid, NOAA Atlas NESDIS, 11, National Oceanic and Atmospheric Administration, Silver Spring, MD, https://repository.library.noaa.gov/view/noaa/1069/noaa_1069_DS1.pdf (last access: 16 June 2026), 1997.
- Boyer, T. P., Antonov, J. I., Baranova, O. K., Coleman, C., Garcia, H. E., Grodsky, A., Locarnini, R. A., Mishonov, A. V., O'Brien, T. D., Paver, C. R., Reagan, J. R., Seidov, D., Smolyar, I. V., and Zweng, M. M.: World Ocean Database 2013, NOAA Atlas NESDIS, 72, <https://repository.oceanbestpractices.org/handle/11329/357> (last access: 16 June 2026), 2013.
- Breiman, L.: Random Forests, *Mach. Learn.*, 45, 5–32, <https://doi.org/10.1023/A:1010933404324>, 2001.
- Breitburg, D., Levin, L. A., Oschlies, A., Grégoire, M., Chavez, F. P., Conley, D. J., Garçon, V., Gilbert, D., Gutiérrez, D., Isensee, K., Jacinto, G. S., Limburg, K. E., Montes, I., Naqvi, S. W. A., Pitcher, G. C., Rabalais, N. N., Roman, M. R., Rose, K. A., Seibel, B. A., Telszewski, M., Yasuhara, M., and Zhang, J.: Declining oxygen in the global ocean and coastal waters, *Science*, 359, eaam7240, <https://doi.org/10.1126/science.aam7240>, 2018.
- Bushinsky, S. M., Emerson, S. R., Riser, S. C., and Swift, D. D.: Accurate oxygen measurements on modified Argo floats using in situ air calibrations, *Limnol. Oceanogr.-Meth.*, 14, 491–505, <https://doi.org/10.1002/lom3.10107>, 2016.
- Bushinsky, S. M., Nachod, Z., Fassbender, A. J., Tamsitt, V., Takeshita, Y., and Williams, N.: Offset Between Profiling Float and Shipboard Oxygen Observations at Depth Imparts Bias on Float pH and Derived pCO₂, *Global Biogeochem. Cy.*, 39, e2024GB008185, <https://doi.org/10.1029/2024GB008185>, 2025.
- Chen, X., Qiu, B., Du, Y., Chen, S., and Qi, Y.: Interannual and interdecadal variability of the North Equatorial Countercurrent in the Western Pacific, *J. Geophys. Res.-Oceans*, 121, 7743–7758, <https://doi.org/10.1002/2016JC012190>, 2016.
- Claustre, H., Johnson, K. S., and Takeshita, Y.: Observing the Global Ocean with Biogeochemical-Argo, *Annu. Rev. Mar. Sci.*, 12, 23–48, <https://doi.org/10.1146/annurev-marine-010419-010956>, 2020.
- D'Asaro, E. A. and McNeil, C.: Calibration and Stability of Oxygen Sensors on Autonomous Floats, *J. Atmos. Ocean. Tech.*, 30, 1896–1906, <https://doi.org/10.1175/JTECH-D-12-00222.1>, 2013.
- Drucker, R. and Riser, S. C.: In situ phase-domain calibration of oxygen optodes on profiling floats, *Meth. Oceanogr.*, 17, 296–318, <https://doi.org/10.1016/j.mio.2016.09.007>, 2016.
- Estapa, M. L., Feen, M. L., and Breves, E.: Direct observations of biological carbon export from profiling floats in the subtropical North Atlantic, *Global Biogeochem. Cy.*, 33, 282–300, <https://doi.org/10.1029/2018GB006098>, 2019.
- Giglio, D., Lyubchich, V., and Mazloff, M. R.: Estimating oxygen in the Southern Ocean using Argo temperature and salinity, *J. Geophys. Res.-Oceans*, 123, 4280–4297, <https://doi.org/10.1029/2017JC013404>, 2018.
- Helm, K. P., Bindoff, N. L., and Church, J. A.: Observed decreases in oxygen content of the global ocean, *Geophys. Res. Lett.*, 38, L23602, <https://doi.org/10.1029/2011GL049513>, 2011.
- Ito, T., Minobe, S., Long, M. C., and Deutsch, C.: Upper ocean O₂ trends: 1958–2015, *Geophys. Res. Lett.*, 44, 4214–4223, <https://doi.org/10.1002/2017GL073613>, 2017.
- Ito, T., Cervania, A., Cross, K., Ainchwar, S., and Delawalla, S.: Mapping dissolved oxygen concentrations by combining shipboard and Argo observations using machine learning algorithms, *J. Geophys. Res.-Machine Learning and Computation*, 1, e2024JH000272, <https://doi.org/10.1029/2024JH000272>, 2024.
- Johnson, K. S., Plant, J. N., Riser, S. C., and Gilbert, D.: Air oxygen calibration of oxygen optodes on a profiling float array, *J. Atmos. Ocean. Tech.*, 32, 2160–2172, <https://doi.org/10.1175/JTECH-D-15-0101.1>, 2015.
- Johnson, K. S., Plant, J. N., Coletti, L. J., Jannasch, H. W., Sakamoto, C. M., Riser, S. C., Swift, D. D., Williams, N. L., Boss, E., Haëntjens, N., Talley, L. D., Sarmiento, J. L., and Gruber, N.: Biogeochemical sensor performance in the SOCCOM profiling float array, *J. Geophys. Res.-Oceans*, 122, 6416–6436, <https://doi.org/10.1002/2017JC012838>, 2017.
- Johnson, K. S. and Bif, M. B.: Constraint on net primary productivity of the global ocean by Argo oxygen measurements, *Nat. Geosci.*, 14, 769–774, <https://doi.org/10.1038/s41561-021-00807-z>, 2021.
- Kalnay, E., Kanamitsu, M., Kistler, R., Collins, W., Deaven, D., Gandin, L., Iredell, M., Saha, S., White, G., Woollen, J., Zhu, Y., Chelliah, M., Ebisuzaki, W., Higgins, W., Janowiak, J., Mo, K. C., Ropelewski, C., Wang, J., Leetmaa, A., Reynolds, R., Jenne, R., and Joseph, D.: The NCEP/NCAR 40-Year Reanalysis Project, *B. Am. Meteorol. Soc.*, 77, 437–471, [https://doi.org/10.1175/1520-0477\(1996\)077<0437:TNYRP>2.0.CO;2](https://doi.org/10.1175/1520-0477(1996)077<0437:TNYRP>2.0.CO;2), 1996.
- Kara, A. B., Rochford, P. A., and Hurlburt, H. E.: An optimal definition for ocean mixed layer depth, *J. Geophys. Res.-Oceans*, 105, 16803–16821, <https://doi.org/10.1029/2000JC900072>, 2000.

- Keeling, R. F., Körtzinger, A., and Gruber, N.: Ocean deoxygenation in a warming world, *Annu. Rev. Mar. Sci.*, 2, 199–229, <https://doi.org/10.1146/annurev.marine.010908.163855>, 2010.
- Kolodziejczyk, N., Portela, E., Thierry, V., and Prigent, A.: ISASO2: recent trends and regional patterns of ocean dissolved oxygen change, *Earth Syst. Sci. Data*, 16, 5191–5206, <https://doi.org/10.5194/essd-16-5191-2024>, 2024.
- Körtzinger, A., Schimanski, J., and Send, U.: High quality oxygen measurements from profiling floats: A promising new technique, *J. Atmos. Ocean. Tech.*, 22, 302–308, <https://doi.org/10.1175/JTECH1701.1>, 2005.
- Kwiatkowski, L., Torres, O., Bopp, L., Aumont, O., Chamberlain, M., Christian, J. R., Dunne, J. P., Gehlen, M., Ilyina, T., John, J. G., Lenton, A., Li, H., Lovenduski, N. S., Orr, J. C., Palmieri, J., Santana-Falcón, Y., Schwinger, J., Séférian, R., Stock, C. A., Tagliabue, A., Takano, Y., Tjiputra, J., Toyama, K., Tsujino, H., Watanabe, M., Yamamoto, A., Yool, A., and Ziehn, T.: Twenty-first century ocean warming, acidification, deoxygenation, and upper-ocean nutrient and primary production decline from CMIP6 model projections, *Biogeosciences*, 17, 3439–3470, <https://doi.org/10.5194/bg-17-3439-2020>, 2020.
- Lauvset, S. K., Lange, N., Tanhua, T., Bittig, H. C., Olsen, A., Kozyr, A., Alin, S., Álvarez, M., Azetsu-Scott, K., Barbero, L., Becker, S., Brown, P. J., Carter, B. R., da Cunha, L. C., Feely, R. A., Hoppema, M., Humphreys, M. P., Ishii, M., Jeansson, E., Jiang, L.-Q., Jones, S. D., Lo Monaco, C., Murata, A., Müller, J. D., Pérez, F. F., Pfeil, B., Schirnack, C., Steinfeldt, R., Suzuki, T., Tilbrook, B., Ulfso, A., Velo, A., Woosley, R. J., and Key, R. M.: GLODAPv2.2022: the latest version of the global interior ocean biogeochemical data product, *Earth Syst. Sci. Data*, 14, 5543–5572, <https://doi.org/10.5194/essd-14-5543-2022>, 2022.
- Li, C., Huang, J., Ding, L., Liu, X., Yu, H., and Huang, J.: Increasing escape of oxygen from oceans under climate change, *Geophys. Res. Lett.*, 47, e2019GL086345, <https://doi.org/10.1029/2019GL086345>, 2020.
- Limburg, K. E., Breitburg, D., Swaney, D. P., and Jacinto, G.: Ocean deoxygenation: A primer, *One Earth*, 2, 24–29, <https://doi.org/10.1016/j.oneear.2020.01.001>, 2020.
- Masumoto, Y., Sasaki, H., Kagimoto, T., Komori, N., Ishida, A., Sasai, Y., Miyama, T., Motoi, T., Mitsudera, H., Takahashi, K., and Sakuma, H.: A fifty-year eddy-resolving simulation of the world ocean: Preliminary outcomes of OFES (OGCM for the Earth Simulator), *Journal of the Earth Simulator*, 1, 35–56, https://www.jamstec.go.jp/es/jp/output/publication/journal/jes_vol.1/pdf/JES1-3.2-masumoto.pdf (last access: 16 June 2026), 2004.
- Masumoto, Y.: Sharing the results of a high-resolution ocean general circulation model under a multi-discipline framework – a review of OFES activities, *Ocean Dynam.*, 60, 633–652, <https://doi.org/10.1007/s10236-010-0297-z>, 2010.
- Maurer, T. L., Plant, J. N., and Johnson, K. S.: Delayed-mode quality control of oxygen, nitrate, and pH data on SOCCOM biogeochemical profiling floats, *Frontiers in Marine Science*, 8, 683207, <https://doi.org/10.3389/fmars.2021.683207>, 2021.
- Nakamura, T. and Awaji, T.: Tidally induced diapycnal mixing in the Kuril Straits and its role in water transformation and transport: A three-dimensional nonhydrostatic model experiment, *J. Geophys. Res.-Oceans*, 109, C09015, <https://doi.org/10.1029/2003JC001850>, 2004.
- Nakamura, T., Awaji, T., Hatayama, T., Akitomo, K., Takizawa, T., Kono, T., and Takahashi, M.: The generation of large-amplitude unsteady lee waves by subinertial K1 tidal flow: A possible vertical mixing mechanism in the Kuril Straits, *J. Phys. Oceanogr.*, 30, 1601–1621, [https://doi.org/10.1175/1520-0485\(2000\)030<1601:TGOLAU>2.0.CO;2](https://doi.org/10.1175/1520-0485(2000)030<1601:TGOLAU>2.0.CO;2), 2000a.
- Nakamura, T., Awaji, T., Hatayama, T., Akitomo, K., and Takizawa, T.: Tidal exchange through the Kuril Straits, *J. Phys. Oceanogr.*, 30, 1622–1644, [https://doi.org/10.1175/1520-0485\(2000\)030<1622:TETTKS>2.0.CO;2](https://doi.org/10.1175/1520-0485(2000)030<1622:TETTKS>2.0.CO;2), 2000b.
- Nicholson, D. P. and Feen, M. L.: Air calibration of an oxygen optode on an underwater glider, *Limnol. Oceanogr.-Meth.*, 15, 495–502, <https://doi.org/10.1002/lom3.10177>, 2017.
- Ogata, T. and Nonaka, M.: Mechanisms of long-term variability and recent trend of salinity along 137°E, *J. Geophys. Res.-Oceans*, 125, e2019JC015290, <https://doi.org/10.1029/2019JC015290>, 2020.
- Pacanowski, R. C. and Griffies, S. M.: MOM 3.0 Manual, Technical Report 4, Geophysical Fluid Dynamics Laboratory, Princeton, NJ, 680 pp., https://mom-ocean.github.io/assets/pdfs/MOM3_manual.pdf (last access: 16 June 2026), 2000.
- Pörtner, H. O. and Farrell, A. P.: Physiology and climate change, *Science*, 322, 690–692, <https://doi.org/10.1126/science.1163156>, 2008.
- Pozo Buil, M. and Di Lorenzo, E.: Decadal dynamics and predictability of oxygen and subsurface tracers in the California Current System, *Geophys. Res. Lett.*, 44, 4204–4213, <https://doi.org/10.1002/2017GL072931>, 2017.
- Reid, J. L.: On the total geostrophic circulation of the Pacific Ocean: flow patterns, tracers, and transports, *Prog. Oceanogr.*, 39, 263–352, [https://doi.org/10.1016/S0079-6611\(97\)00012-8](https://doi.org/10.1016/S0079-6611(97)00012-8), 1997.
- Roemmich, D. and Gilson, J.: The 2004–2008 mean and annual cycle of temperature, salinity, and steric height in the global ocean from the Argo Program, *Prog. Oceanogr.*, 82, 81–100, <https://doi.org/10.1016/j.pocean.2009.03.004>, 2009.
- Sampaio, E., Santos, C., Rosa, I. C., Ferreira, V., Pörtner, H.-O., Duarte, C. M., Levin, L. A., and Rosa, R.: Impacts of hypoxic events surpass those of future ocean warming and acidification, *Nature Ecology & Evolution*, 5, 311–321, <https://doi.org/10.1038/s41559-020-01370-3>, 2021.
- Sasaki, H., Nonaka, M., Masumoto, Y., Sasai, Y., Uehara, H., and Sakuma, H.: An eddy-resolving hindcast simulation of the quasiglobal ocean from 1950 to 2003 on the Earth Simulator, in: *High Resolution Numerical Modelling of the Atmosphere and Ocean*, edited by: Hamilton, K. and Ohfuchi, W., Springer, New York, NY, 157–185, https://doi.org/10.1007/978-0-387-49791-4_10, 2008.
- Sasano, D., Takatani, Y., Kosugi, N., Nakano, T., Midorikawa, T., and Ishii, M.: Multidecadal trends of oxygen and their controlling factors in the western North Pacific, *Global Biogeochem. Cy.*, 29, 935–956, <https://doi.org/10.1002/2014GB005065>, 2015.
- Sasano, D., Takatani, Y., Kosugi, N., Nakano, T., Midorikawa, T., and Ishii, M.: Decline and biennial oscillations of dissolved oxygen in the Oyashio region and their propagation to the western North Pacific, *Global Biogeochem. Cy.*, 32, 909–931, <https://doi.org/10.1029/2017GB005876>, 2018.
- Schmidtko, S., Stramma, L., and Visbeck, M.: Decline in global oceanic oxygen content during the past five decades, *Nature*, 542, 335–339, <https://doi.org/10.1038/nature21399>, 2017.

- Sharp, J. D., Fassbender, A. J., Carter, B. R., Johnson, G. C., Schultz, C., and Dunne, J. P.: GOBAI-O₂: A Global Gridded Monthly Dataset of Ocean Interior Dissolved Oxygen Concentrations Based on Shipboard and Autonomous Observations (NCEI Accession 0259304), NOAA National Centers for Environmental Information [data set], <https://doi.org/10.25921/z72m-yz67>, 2022.
- Sharp, J. D., Fassbender, A. J., Carter, B. R., Johnson, G. C., Schultz, C., and Dunne, J. P.: GOBAI-O₂: temporally and spatially resolved fields of ocean interior dissolved oxygen over nearly 2 decades, *Earth Syst. Sci. Data*, 15, 4481–4518, <https://doi.org/10.5194/essd-15-4481-2023>, 2023.
- Stramma, L., Schmidtko, S., Bograd, S. J., Ono, T., Ross, T., Sasano, D., and Whitney, F. A.: Trends and decadal oscillations of oxygen and nutrients at 50 to 300 m depth in the equatorial and North Pacific, *Biogeosciences*, 17, 813–831, <https://doi.org/10.5194/bg-17-813-2020>, 2020.
- Stramma, L. and Schmidtko, S.: Tropical deoxygenation sites revisited to investigate oxygen and nutrient trends, *Ocean Sci.*, 17, 833–847, <https://doi.org/10.5194/os-17-833-2021>, 2021.
- Suga, T., Takei, Y., and Hanawa, K.: Thermostad distribution in the North Pacific subtropical gyre: The central mode water and the subtropical mode water, *J. Phys. Oceanogr.*, 27, 140–152, 1997.
- Suga, T., Motoki, K., Aoki, Y., and Macdonald, A. M.: The North Pacific climatology of winter mixed layer and mode waters, *J. Phys. Oceanogr.*, 34, 3–22, 2004.
- Takatani, Y., Sasano, D., Nakano, T., Midorikawa, T., and Ishii, M.: Decrease of dissolved oxygen after the mid-1980s in the western North Pacific subtropical gyre along the 137°E repeat section, *Global Biogeochem. Cy.*, 26, GB2013, <https://doi.org/10.1029/2011GB004227>, 2012.
- Takeshita, Y., Martz, T. R., Johnson, K. S., Plant, J. N., Gilbert, D., Riser, S. C., Neill, C., and Tilbrook, B.: A climatology-based quality control procedure for profiling float oxygen data, *J. Geophys. Res.-Oceans*, 118, 5640–5650, <https://doi.org/10.1002/jgrc.20399>, 2013.
- Udaya Bhaskar, T. V. S., Sarma, V. V. S. S., and Pavan Kumar, J.: Potential mechanisms responsible for spatial variability in intensity and thickness of oxygen minimum zone in the Bay of Bengal, *J. Geophys. Res.-Biogeo.*, 126, e2021JG006341, <https://doi.org/10.1029/2021JG006341>, 2021.
- Winkler, L. W.: Die Bestimmung des im Wasser gelösten Sauerstoffes, *Ber. Dtsch. Chem. Ges.*, 21, 2843–2854, <https://doi.org/10.1002/cber.188802102122>, 1888.
- Wolf, M. K., Hamme, R. C., Gilbert, D., Yashayaev, I., and Thierry, V.: Oxygen saturation surrounding deep water formation events in the Labrador Sea from Argo-O₂ data, *Global Biogeochem. Cy.*, 32, 635–653, <https://doi.org/10.1002/2017GB005829>, 2018.
- Xu, L., Wang, K., and Wu, B.: Weakening and poleward shifting of the North Pacific subtropical fronts from 1980 to 2018, *J. Phys. Oceanogr.*, 52, 399–417, <https://doi.org/10.1175/JPO-D-21-0170.1>, 2022.
- Yang, H., Lohmann, G., Krebs-Kanzow, U., Ionita, M., Shi, X., Sidorenko, D., Gong, X., Chen, X., and Gowan, E. J.: Poleward shift of the major ocean gyres detected in a warming climate, *Geophys. Res. Lett.*, 47, e2019GL085868, <https://doi.org/10.1029/2019GL085868>, 2020.
- Yasuda, I.: North Pacific Intermediate Water: Progress in SAGE (SubArctic Gyre Experiment) and related projects, *J. Oceanogr.*, 60, 385–395, <https://doi.org/10.1023/B:JOCE.0000038344.25081.42>, 2004.
- You, Y.: The pathway and circulation of North Pacific Intermediate Water, *Geophys. Res. Lett.*, 30, 2291, <https://doi.org/10.1029/2003GL018561>, 2003.